This is a repository copy of *Synthesis and Characterisation of Analogues for Interplanetary Dust and Meteoric Smoke Particles*.

1 # Synthesis and Characterisation of Analogues for

2 # Interplanetary Dust and Meteoric Smoke Particles

3 Alexander D. James[a], Victoria L. F. Frankland[a], Josep M. Trigo-Rodríguez[b], Jacinto

4 Alonso-Azcárate[c], Juan Carlos Gómez Martín[a], and John M. C. Plane[a*]

5 [a] *School of Chemistry, University of Leeds, Leeds, LS2 9JT, UK*

6 [b] *Meteorites, Minor Bodies and Planetary Science Group, Institute of Space Sciences (CSIC-*

7 *IEEC). Campus UAB, C/ Can Magrans s/n, 08193 Cerdanyola del Vallés (Barcelona), Spain*

8 [c] *Universidad de Castilla-La Mancha (UCLM), Campus Fábrica de Armas, 45071 Toledo,*

9 *Spain.*

10 *corresponding author: j.m.c.plane@leeds.ac.uk

11 **Abstract**

12 Analogues have been developed and characterised for both interplanetary dust and

13 meteoric smoke particles. These include amorphous materials with elemental compositions

14 similar to the olivine mineral solid solution series, a variety of iron oxides, undifferentiated

15 meteorites (chondrites) and minerals which can be considered good terrestrial proxies to

16 some phases present in meteorites. The products have been subjected to a suite of

17 analytical techniques to demonstrate their suitability as analogues for the target materials.

18 Keywords: Interplanetary Dust; Meteoric Smoke; Micrometeorites; Sol-gel synthesis

19 **1. Introduction**

20 Many processes in atmospheric environments are controlled by the availability of reactive

21 or catalytic surfaces which originate from outside that atmosphere (Nachbar, et al., 2016,

22 Petrie, 2004, Plane, 2012, Turco, et al., 1981). However, this extraterrestrial material is only

23 partially characterised and understood in terms of these various atmospheric processes.

24 Meanwhile, collecting the relatively large quantities required for surface science

25 experiments (often grams to kilograms) from the atmosphere presents an extremely large

26 engineering challenge (Hedin, et al., 2014). In order to investigate and understand such

27 atmospheric processes, it is therefore vital to employ suitable analogue materials which will

28 mimic the behaviour of the environmental material.

29 The majority of dust which enters planetary atmospheres in our solar system originates

30 from either Jupiter Family Comets (JFCs), the Asteroid Belt (AB), Halley Type Comets (HTCs)

31 or Oort Cloud Comets (OCCs) (Nesvorný, et al., 2011, Nesvorný, et al., 2010). To determine

32 the appropriate material to mimic the atmospheric behaviour of Interplanetary Dust

33 Particles (IDPs), the nature of such dust before encountering an atmosphere and the

34 processes it will undergo during atmospheric entry must be considered.

1.1. Composition, morphology and size distribution of Interplanetary Dust

The primary source of information about the composition and morphology of IDPs are the large collections of micrometeorites retrieved in the stratosphere (Rietmeijer, 2000, Zolensky and Lindstrom, 1992), the ice caps (Maurette, et al., 1987, Taylor, et al., 1998), deserts (Kohout, et al., 2014) and deep sea sediments (Blanchard, et al., 1980). While these collections include particles exhibiting different degrees of thermal alteration (ranging from unmelted particles to cosmic spherules) and weathering, it has been possible to establish their general properties before aerobraking (Jessberger, et al., 2001, Kohout, et al., 2014, Taylor, et al., 2012). IDPs size and composition have also been investigated by particle detectors on board orbital spacecraft such as the Long Duration Exposure Facility (LDEF) (Love and Brownlee, 1993) and the MIR Space Station (Hörz, et al., 2000), where the major difficulty has been characterising the effect of the high speed impacts (v >11 km s^{-1}) on the exposed materials (e.g. aluminium, aerogel). Several past and ongoing space missions such as Stardust (Hörz, et al., 2006), Deep Impact (Lisse, et al., 2006) and Rosetta (Schulz, et al., 2015) have gathered information close to cometary sources of dust. Stardust is the only mission to date which captured dust particles ejected from a comet (81P Wild 2) and, after deceleration and disruption in the aerogel (SiO$_2$) collector (Trigo-Rodríguez and Llorca, 2007), returned them to Earth. Study of the aerogel keystones has allowed a thorough laboratory chemical and mineralogical characterisation of the particles (Frank, et al., 2014, Stephan, et al., 2008). Rosetta currently analyses *in situ* the composition, morphology and optical properties of particles released by comet 67P Churyumov-Gerasimenko (Hilchenbach, et al., 2016). A caveat to these close-to-source studies is that a particular comet is only a sample among a population of millions. Comparison of Antarctic micrometeorites and Stardust samples shows clear similarities, but also differences (Dobrică, et al., 2009). Astronomical observations and modelling have provided key information about the spatial distribution, the sources and the size distribution of the interplanetary dust forming the so-called Zodiacal Cloud (Ade, et al., 2014, Fixsen and Dwek, 2002, Nesvorný, et al., 2011).

The meteoroid particles which contribute most to the meteoric input to the Earth's atmosphere are 10-50 µm in radius (0.01 to 1 µg assuming 3 g cm^{-3} density) (Carrillo-Sánchez, et al., 2015, Nesvorný, et al., 2011). The analysis of the Antarctic collections has shown that IDPs are consistent with the Carbonaceous Ivuna (CI) chondritic composition, while mineralogically IDPs are closer to the Carbonaceous Mighei (CM) chondritic composition (Jessberger, et al., 2001, Taylor, et al., 2012). Analysis of the more than 5000 micrometeorite (MM) particles of the 2000 South Pole Water Well collection, described by Taylor, et al. (2012), indicates that ~75% of IDPs are fine grained aggregates of CI-CM elemental composition, 10% coarse grain anhydrous minerals and less than 10% ordinary chondrites (OC). Less than 1% of the MMs have achondritic compositions, CAI components, or recognizable chondrules. Besides the low abundance of OC IDPs, they also show important compositional and morphologically differences with respect to carbonaceous

75   chondritic (CC) meteorites. IDPs are extremely fine-grained aggregates, such that despite of
76   the mineralogical heterogeneity of the sub-micron sized grains, the bulk chemistry matches
77   CI and CM composition as a whole. By contrast, the matrix of carbonaceous meteorites is
78   composed of micron-sized coarse grained aggregates, single mineral grains, chondrules,
79   etc., and therefore a section of a meteorite of the same size of an IDP frequently does not
80   match the bulk elemental composition (Jessberger, et al., 2001). The porosity of IDPs is in
81   line with that of CI and CM meteorites, with bulk densities around 2 g cm^{-3} (Jessberger, et
82   al., 2001). OC meteorites have bulk densities higher than 3 g cm^{-3} because they have
83   experienced mild thermal metamorphism that reduces the pores (Consolmagno, et al.,
84   2008).

1.2.   Ablation on Atmospheric Entry

86   Upon encountering an atmosphere IDPs heat frictionally, often to the point of melting and
87   evaporating, forming a meteor. Ablation occurs both through sputtering by atmospheric
88   and, if the particle melts, rapid evaporation of the constituent elements. This process is
89   known as meteoric ablation. The majority of the incoming particles are too small to
90   generate visually detectable meteoroids (particles need to be larger than 1 mm radius), but
91   ionization of the ablated atoms by hyperthermal collisions with atmospheric molecules
92   forms electrons which enable detection by radar, either through specular reflection from
93   the resulting electron trail or by incoherent scatter from the ball of electrons around the
94   meteoroid – termed the head echo (e.g. (Janches, et al., 2009)). The ablation rate of a
95   particular meteoroid is a function of its mass, entry velocity and incident angle (Vondrak, et
96   al., 2008). Furthermore, the different melting points and volatilities of the various
97   components of meteoroids result in a process known as differential ablation, whereby the
98   most volatile components ablate first (Janches, et al., 2009, Trigo-Rodríguez and Llorca,
99   2007, Vondrak, et al., 2008). An unablated particle will then sediment through the
100   atmosphere under gravity and, if small enough (<1 μm for Earth) be transported by the
101   general atmospheric circulation and eventually reach the surface, where it is termed a
102   micrometeorite (MM). Partially ablated material has been identified on the Earth's surface
103   in the form of scoriaceous MMs and cosmic spherules, (which form when a particle melts
104   but does not completely ablate) (Blanchard, et al., 1980, Kohout, et al., 2014, Taylor, et al.,
105   1998). The vaporized elements give rise to the layers of metallic atoms and ions in the
106   mesosphere and lower themosphere (Plane, et al., 2015).

1.3.   Meteoric Smoke Formation and properties

108   The atmospheric chemistry of meteor-ablated metals depends on the atmosphere in
109   question (Plane, et al., 2015, Whalley and Plane, 2010). Gas-phase reactions produce stable
110   reservoirs which can then polymerise into nanoparticles known as meteoric smoke particles
111   (MSPs) (Hunten, et al., 1980, Plane, 2003). In general the most stable reservoir for a metal,
112   and therefore the composition of MSP, will depend on the reactivity of that metal and its
113   derivatives with O_3 and O_2 to give oxides, H_2O to give hydroxides, $Si(OH)_4$ and SiO_2 to give

114 silicates and CO_2 to give carbonate and bicarbonates, as well as the stability of these
115 compounds with respect to O and H atom reactions which reduce them back to metal atoms
116 (Plane, et al., 2015). Based on laboratory experiments MSPs should then grow by rapid
117 agglomeration as they are transported through an atmosphere (Saunders and Plane, 2006).
118 In the case of the Earth's atmosphere, MSPs are modelled to reach a radius of around 100
119 nm in the stratosphere (Bardeen, et al., 2008).

120 Here MSPs and IDPs are collectively referred to as meteoric material. Particles collected by
121 aircraft in the stratosphere are often termed IDPs (Bigg, 2012), whilst those collected at the
122 surface are labelled MMs (Taylor, et al., 2012). In order to determine the most appropriate
123 analogue material, the key difference is between ablated and unablated material. In this
124 paper, IDPs should be taken to refer to unablated material, MSPs to ablated matter, and
125 MMs specifically to unablated material which sediments to the surface.

126 MSPs have been detected in a variety of ways. In the Earth's atmosphere MSPs occur in a
127 weak plasma and so a small fraction are charged by electron attachment, which enables
128 them to be detected using rocket-borne Faraday cup detectors (Plane, et al., 2014, Rapp, et
129 al., 2012, Robertson, et al., 2014). These detectors can be coupled to photo-ionisation flash
130 lamps so that neutral particles can be detected simultaneously (Rapp, et al., 2012).
131 However, attempts to capture and return MSPs for detailed analysis have had very limited
132 success so far (Hedin, et al., 2014). Particles consisting of compact and chain aggregates
133 have been retrieved from the upper stratosphere and the mesosphere (Bigg, 2012, Farlow,
134 et al., 1970, Witt, et al., 1964). The chain aggregates are reminiscent of fractal-like
135 laboratory-generated analogues (Saunders and Plane, 2006), but direct identification and
136 characterisation of MSPs particles has been largely inconclusive. MSPs have also been
137 observed by measuring their optical extinction using the SOFIE spectrometer on the AIM
138 satellite (Russell, et al., 2009)), but the composition of the particles are not well constrained
139 (Hervig, et al., 2009). Observations of polar mesospheric clouds by SOFIE indicate the
140 presence of MSPs in the cloud ice particles that could be consistent with wüstite (FeO), or
141 magnesiowüstite ($Mg_xFe_{1-x}O$, x= 0.1 – 0.6). Such investigation is limited by the knowledge of
142 refractive indexes, with comparison only possible to bulk, crystalline materials. The likely
143 amorphous nature of MSPs (Saunders and Plane, 2011) and further their fractal-like
144 morphology significantly complicates understanding of their extinction properties
145 (Sorensen, 2001).

1.4.   Impacts of Meteoric Materials

147 The potential impacts of meteoric materials – both unablated material and MSPs - can be
148 grouped into three categories. First is the removal of acids such as H_2SO_4 and HNO_3
149 (Frankland, et al., 2015, Saunders, et al., 2012), which undergo acid-base reactions with the
150 metallic species in the particles. Second is the particles providing surfaces for
151 heterogeneous chemistry, including the conversion of HO_2 into H_2O_2 in the Earth's
152 stratosphere (James, et al., 2016 - Unpublished results), the cyclo-trimerization of C_2H_2 into

153   C_6H_6 in Titan's troposphere (Frankland, et al., 2016 - in press), and the oxidation of CO in
154   Venus's lower atmosphere (Frankland, et al., 2016 - Unpublised results). Third is the
155   particles acting as heterogeneous nuclei, either *via* direct deposition of a supersaturated
156   vapour such as H_2O or CO_2 onto the meteoric particles (Nachbar, et al., 2016, Plane, 2011),
157   or *via* immersion of the particles in a liquid droplet, such as a H_2SO_4 droplet in the Earth's
158   stratosphere (Hoyle, et al., 2013).

159   Although the radiative forcing of MSPs is almost certainly negligible under present day
160   conditions, MSPs may have played a larger climactic role during the Earth's early history
161   (Saunders, et al., 2007). In any case, MSP extinction needs to be taken into account when
162   interpreting optical extinction measurements in the upper stratosphere (Neely, et al., 2011).

163   Investigating this wide range of processes involving extraterrestrial material requires access
164   to appropriate analogues in the laboratory. In this paper the synthesis and characterisation
165   of a number of analogues for IDPs and MSPs is reported and compared to those in the
166   literature. The main aim of this study is therefore to lay the groundwork for future studies
167   which can quantify the various impacts of meteoric material in planetary atmospheres. The
168   paper is intended for atmospheric scientists, to introduce concepts which largely come from
169   the field of meteoritics, and to aid the choice of materials in future studies of atmospheric
170   processes.

171   **2.   Preparation of Analogues**

172   Analogues have been prepared both by processing mineral and meteorite samples, and by
173   chemical synthesis from appropriate precursors. The genesis of the various samples is
174   described in Table 1 along with their proposed application, specific surface area and mass
175   density as appropriate. Note that throughout this text any crystalline materials will be
176   referred to by their names, whilst chemical compositions will be used for materials without
177   significant crystal structure.

178   **2.1.   Meteoritic Material**

179   Samples of the Allende (CV3) (Clarke, et al., 1971), Murchison (CM2) (Fuchs, et al., 1973),
180   North West Africa 5515 (NWA, CK4) (Weisberg, et al., 2009) and Chergach (H5) (Weisberg,
181   et al., 2008) meteorites were ground by hand using a pestle and mortar and then sieved
182   (Endecottes test sieves, pore sizes of 38, 106, 150, 250 and 355 μm) to obtain size fractions
183   relevant for use as IDP analogues (tens to hundreds of μm radius (Bardeen, et al., 2008,
184   Bigg, 2012, Carrillo-Sánchez, et al., 2015)). These meteorites represent several carbonaceous
185   groups and one ordinary chondrite. Allende and Murchison have notably been used in a
186   number of previous studies investigating IDP behaviour whilst NWA and Chergach have
187   been included to represent outlier groups in the likely IDP flux (see Section 3.6.) (Burchell, et
188   al., 2006, Court and Sephton, 2011, Toppani, et al., 2001).

189 **2.2   Terrestrial Minerals**

190 Terrestrial minerals were also used here as analogues for fine and coarse-grained anhydrous

191 IDP material. These were obtained by grinding peridot olivine, labradorite, anorthite and

192 albite followed by size separation. These minerals were chosen as example members of

193 solution series. Other members of such series or other minerals could also be used, either

194 alone or in mixtures, to obtain a wider range of compositions. Similar terrestrial minerals

195 have been used in the past to investigate IDP processing. These include simulated changes

196 in pyrrhotites during aerobraking e.g. (Greshake, et al., 1998) and olivine and pyroxene as a

197 "thermometer" for the temperatures reached by meteors (Sandford and Bradley, 1989).

198 **2.3   Synthetic Samples**

199 Sol-gel synthetic routes to produce both crystalline mineral samples and amorphous

200 materials of suitable composition were also used. Directly synthesised compounds include

201 amorphous materials with compositions covering the olivine solid solution series

202 ($Mg_xFe_{2-x}SiO_4$ where $0 \leq x \leq 2$) and goethite. These can be annealed to produce secondary

203 products including hematite and mixtures of crystalline phases such as enstatite and

204 hematite.

205 $Mg_xFe_{2-x}SiO_4$ compounds were synthesised by stirring at room temperature for 7 days a

206 mixture of stoichiometric amounts (relative to 0.1 mol l^{-1} product) of $MgCl_2$ (Aldrich),

207 $Fe(SO_4)_2(NH_4)_2$ (Sigma-Aldrich) and Na_4SiO_4 (Alfa Aesar) (Frankland, et al., 2015). Solutions

208 immediately turn blue when Fe is present but otherwise are colourless. All solutions are

209 viscous but do not pass the inversion test. After purification, annealing of this amorphous

210 product at 1273 K for 24 hours was also used to generate a mixture crystalline enstatite and

211 hematite.

212 Here we report a novel method to produce pure goethite and, by processing this, hematite.

213 Goethite was obtained by stirring a solution of 0.1 mol l^{-1} each of $Fe(SO_4)_2(NH_4)_2$ and NaOH

214 for 3 days with a flow of compressed air bubbling through the reacting solution. The purified

215 goethite product of this reaction was dehydrated by annealing at 573 K for 24 hours to

216 produce hematite. All products of room temperature reactions were collected and dried in

217 petri dishes. Residual byproducts were removed using repeated dialysis (at least 15 hours

218 total) in a Soxhlet apparatus with the particles held in water permeable tubing (Snakeskin

219 7000 MWCO).

220 Purified products, along with samples of meteoritic and terrestrial materials were then

221 subjected to a suite of characterisation techniques in order to assess their appropriateness

222 as analogues for IDPs and MSPs. Mass yields after purification are >90 %, although the

223 possibility that H_2O is adsorbed to the large surface area of the synthetic particles adds an

224 upward bias to such measurements. In any case, approximately 20 g of $Mg_xFe_{2-x}SiO_4$ and

225 3-5 g goethite can be produced in a typical 2 l batch synthesis, providing sufficient material

226 for characterisation and further studies.

3. Characterisation of Analogues

A thorough characterisation of each of the products described above is required to inform their use as analogues for IDPs and/or MSPs. The properties which are required for a given analogue depend on the application to which it is put. This is compounded by the differing size scales of IDPs (up to several tens to hundred μm radius) and MSPs (single molecules which polymerise and agglomerate to several hundred nm radius), which restricts somewhat the techniques available for the characterisation of each analogue.

Where ablation is examined, it is important to understand the elemental composition and crystal structure, particularly as this has implications for melting and evaporation. In studies of catalysis, however, the surface properties of a sample are of paramount importance. Such properties have been investigated for samples of the products discussed in Section 2.

3.1. Elemental composition

The elemental composition of a material has clear relevance to studies of virtually all properties of meteoric material, and is arguably the most widely applicable characterisation of both environmental and analogue samples. Taylor, et al. (2012) examined around 5000 MMs from the South Polar Water Well and showed that IDPs have likely compositions similar to CI or CM meteorites. Whilst there is considerable uncertainty in the mineral composition of MSPs e.g. (Hervig, et al., 2012), the elemental ratios of the metals (primarily Fe, Mg) and SiO_2 available for their formation are relatively well known (Plane, et al., 2015).

Elemental compositions were measured by Energy Dispersive X-Ray Spectroscopy in combination with Scanning Electron Microscopy (SEM-EDX, Joel JSM 6610LV coupled to an Oxford Instruments INCA X max80 EDS). The carbon signal is omitted due to interference from carbon tape used as an SEM substrate, while the oxygen signal is affected by surface adsorbed water. This technique is limited by statistical uncertainty, since values are measured for individual particles or agglomerates rather than large, representative samples, and by reduced sensitivity to lighter elements. Average values with a 95% standard error (typically from 4-8 measurements) are therefor listed. Inductively Coupled Plasma – Atomic Emission Spectroscopy (ICP-AES, ICAP 6500 ThermoElectron) has been used for two meteoritic samples. Solutions were prepared from approximately 0.025 g of each sample fluxed with 0.05 g of Li-metaborate and dissolved in 30 ml HNO_3 1 molal and 1 drop of HF. Four standard reference materials provided by the US Geological Survey were used for external calibration; internal calibration of the equipment was carried out before the measurements and rhodium was used as internal standard. Three determinations of the elemental composition were carried out and averaged for each meteorite, showing standard errors lower than 5% for most elements.

3.1.1. Meteoric Material

Several size fractions (particles of <19 μm and >177.5 μm radii) of the Chergach and NWA (particles of 19-53 μm and 125-177.5 μm radii) meteorites were analysed by SEM-EDX. The

265 composition of the Allende and Murchison meteorite samples were measured by ICP-AES.
266 Elemental compositions of all four meteorites are compared to CI, CM composition and to
267 their respective groups (Hutchison, 2004) in Figure 1. Note that the differences between
268 standard compositions are generally smaller than the standard errors in the compositions.
269 This is due to the coarse grained nature of meteorites in general. After grinding, grains of
270 individual minerals distort the measured composition away from the mean of a larger
271 sample.

272 The Chergach meteorite, shown in Figure 1 a), Si, Cr, Mn, Mg, Ca, K and P all agree within
273 error with the standard compositions. Na and Al are enhanced (although Al is in agreement
274 with the CM compositions) suggesting that the sample contained albite. Fe, Ni and S are
275 depleted, suggesting that minor phases such as Fe-Ni metallic alloys and metal sulfides or
276 sulfates are underrepresented in the sample. The Chergach meteorite has a rather Mg rich
277 olivine content, with much of the Fe being contained in a metallic or alloy form, consistent
278 with an enhancement of major phases over minor in these measurements (Weisberg, et al.,
279 2008). Differences in the two size fractions are generally smaller than the uncertainty.
280 However major constituent elements are enhanced in the smaller size fractions, whilst
281 minor elements are depleted. This suggest that some softer phases are enhanced in the
282 smaller size fractions, whilst phases which grind less easily are enhanced in larger size
283 fractions. There is also a potential effect of particle size; since a flat surface is required for
284 quantitative measurements, single particles are used and measurements of the smaller size
285 fractions therefore survey less material. This could lead to an underrepresentation of rare
286 component phases and elements. In compositional terms, therefore, Chergach (and
287 potentially other OCs) are a reasonable approximation for IDPs. This is significant since OCs
288 are generally more available than CCs.

289 The Murchison and Allende meteorites, shown in Figure 1b), have been included here as
290 examples of carbonaceous chondrites which are commonly used as analogues for IDPs
291 (Burchell, et al., 2006, Court and Sephton, 2011, Toppani, et al., 2001). Allende has suffered
292 some degree of thermal metamorphism so has compositions within the CI-CM range for all
293 elements except Mg, Na and K. The Allende meteorite is known to have an Fe rich olivine
294 matrix, accounting for the Mg depletion. The low abundance of relatively volatile elements
295 such as Na and K is typical of CV meteorites but is known to be extreme in the case of
296 Allende (Clarke, et al., 1971). However, these elemental constituents and their relatively
297 volatile phases (melting points <1500 K) are present in all samples observed. The Murchison
298 sample agrees well with the CI or CM elemental composition, a fact which, combined with
299 its relatively large available mass (>100 kg) has led to its wide use as an IDP analogue.

300 The 125-177.5 μm radius size fraction of the NWA meteorite sample, shown in Figure 1 c), is
301 significantly enriched in Ca and depleted in Na. In addition minor elements including Ti, Mn,
302 K, P, Co and S are below the limit of detection. In the 19-53 μm radius size fraction, SEM-
303 EDX analysis shows a highly heterogeneous composition, with each particle appearing to
304 represent a single phase (elemental ratios consistent with Andesine, Olivine and Augite

305 were observed). This suggests a large content of refractory (melting point >2000 K) and
306 coarse grained components, inconsistent with the bulk of the IDP flux. This highlights the
307 fact that not all CC meteorites are inherently suitable as IDP analogues. Such materials can
308 be useful, however for examining extreme events, e.g. differential ablation of particles with
309 large entry velocities.

310 Ground meteorites are therefore variably suitable analogues for IDPs in terms of elemental
311 composition, however they do contain many relevant phases (see section 3.2.1) and since
312 the ablation process is dominantly controlled by the melting point of the phase (Vondrak, et
313 al., 2008), should act as satisfactory analogues in particular cases.

3.1.2. Terrestrial Material

315 Peridot olivine, labradorite, anorthite and albite samples have also been subjected to
316 SEM-EDX analysis. The olivine was found to be Fo_{90} forsterite (ratios of Mg:Fe = 10 ± 4 and
317 (Fe+Mg):Si = 1.9 ± 0.6) with some content of Ni, Ca and Al, consistent with the volcanic
318 basalt casing around the peridot in which the olivine formed. The labradorite was measured
319 as having An_{55} composition (ratios of Na:Ca = 0.8 ± 0.2 and (Na+Ca):(Si+Al) = 0.244 ± 0.014).
320 The anorthite sample was found to have An_{97} composition (ratios of Na:Ca = 0.04 ± 0.02 and
321 (Na+Ca):(Si+Al) = 0.244 ± 0.014). The albite sample was found to have a composition
322 consistent with such a sodium feldspar (ratios of Al:Si = 0.344 ± 0.013 and
323 Na:Si = 0.33 ± 0.04). The reproducibility (standard errors typically <20 %) of these
324 measurements and their agreement with expected ratios for each mineral support the use
325 of the SEM-EDX characterisation technique so long as numerous spectra are measured for
326 each sample.

3.1.3. Synthetic samples

328 SEM-EDX has been used extensively here to assess the composition of the synthetic
329 products, particularly with regards to the removal of NaCl and Na_2SO_4 salt byproducts. In
330 general it was found that around 10 hours of processing in the Soxhlet apparatus was
331 sufficient to remove these byproducts. This validates the synthesis described above.
332 Subsequent to the purification process, compositions were confirmed for goethite (Fe:O =
333 0.6 ± 0.4), hematite (Fe:O = 0.7 ± 0.3), Mg_2SiO_4 (Mg:Si = 2.0 ± 0.5) and Fe_2SiO_4 (Fe:Si = 2.4 ±
334 0.8). When a ratio of precursors designed to produce $MgFeSiO_4$ was used, a ratio of Mg:Fe =
335 0.43 ± 0.12 and (Fe+Mg):Si = 1.8 ± 0.3 was measured. The overabundance of Fe can partially
336 be explained by the presence of a ferrihydrite or goethite impurity (see section 3.2.2.);
337 however, since the ratio of Fe+Mg to Si is not less than 2 it is possible that Mg
338 accommodation into the synthetic $Mg_xFe_{2-x}SiO_4$ is less effective than that of Fe. This
339 measured composition did not significantly vary on annealing to enstatite / hematite.

340 Note that oxygen ratios are reported for the crystalline iron oxides, but not for amorphous
341 silicates. This is due to contamination by surface adsorbed H_2O in the case of the amorphous
342 silicates, despite storing the samples in a vacuum dessicator for several weeks prior to

343   composition measurements. This is thought to be due to the relatively large surface area of
344   the silicate materials with respect to the iron oxides (hundreds as opposed to several $m^2\,g^{-1}$
345   respectively, see Table 1 and Section 3.3). For applications where surface reactivity is
346   important, this surface water could be removed by heating in a vacuum, though potential
347   phase changes in the dust by such annealing should be considered where this is carried out
348   (see section 3.2). In generally, target compositions could be successfully synthesised and
349   assayed using the techniques described here. Of the elements described here, Fe is the
350   most abundant in Earth's atmosphere. Mg and Si have a slightly lower abundance with Na, K
351   etc. present in smaller amounts (Plane, et al., 2015). Elementally then, these materials
352   therefore represent suitable compositional analogues for MSPs.

3.2.   Textural analysis and compositional maps

354   The homogeneity of analogues is one of the key differences between ground bulk samples
355   and IDPs. This can be evident in the elemental or mineralogical composition of the analogue
356   material. Particle topography and homogeneity, both within each particle and across whole
357   samples, was assessed using SEM-EDX mapping (FEG-SEM – FEI Nova 450) with EDX
358   (AMTEK) at 18 kV) for the Chergach and Allende meteorites. Particles forming the Allende
359   CV3 carbonaceous chondrite are heterogeneous even to the naked eye, with some white
360   and some rounded glassy particles evident. These correspond respectively with Ca- and
361   Al-rich inclusions and chondrules. Chergach particles, on the other hand, appear more
362   homogeneous within each size fraction because of the recrystallization shown in this
363   petrologic type (H5) of ordinary chondrites. These trends hold through to the microscopic
364   scale, as demonstrated by the following analysis.

365   Figure 2 shows a micrograph and co-located compositional maps for a particle of Chergach.
366   The Mg rich olivine matrix is clearly demonstrated, with smaller grains of a variety of phases
367   evident. These potentially include metallic Fe (top left, bottom centre) albite / feldspar
368   (regions with Na and Ca).

369   Figure 3 shows a wide angle micrograph of a large section of the Allende meteorite before
370   grinding. Large features (100s of μm) are visible including a barred olivine chondrule (A), a
371   porphyritic olivine chondrule (B), the fine grained carbonaceous matrix (C) and a metal
372   sulfide inclusion (D). The scale of this image makes it clear that, while the mean of a large
373   sample of particles may be a CI or CM (or in this case CV) composition as are IDPs, a ground
374   sample of the meteorite will contain an overabundance of coarse and simple mineral grains,
375   which would be representative of only a small fraction of IDPs.

376   Figure 4 shows an aggregate particle of Allende, where a region of scoreacious material is in
377   contact with a fine grained region (boundary marked by a dashed white line). EDX mapping,
378   performed on the region shown by the white box on the micrograph, shows that the
379   scoreacious region is depleted in volatile elements such as S, likely indicating loss of volatile
380   phases such as troilite or more likely metal sulfate (Burgess, et al., 1991). The fine grained
381   region also shows a more heterogeneous content, with some Ca containing domains

382   evident. This suggests that the right-hand region has undergone significantly more heating,

383   sufficient for volatile phases to evapourate and leave only the anhydrous metal silicate

384   content. The left-hand region, however, has undergone less thermal alteration and

385   resembles more closely a fine grained IDP.

386   Figure 5 shows two grains of Allende, one single mineral grain (left) and one fine aggregate

387   (right). The single mineral particle appears to be a sodalite or nepheline (sodium silicate,

388   albite is not present in significant quantities in the Allende meteorite (Clarke, et al., 1971)).

389   The fine grained aggregate demonstrates the Fe rich olivine matrix of the Allende meteorite,

390   with a heterogeneous content of Na, Al, Ca and some detectable Ni.

391   These examples have been selected to provide a flavour of the variability in the chondrites

392   examined here. Such heterogeneous compositions are common in IDPs, however the fine

393   grained nature of the majority of IDPs means that large grains such as those observed here

394   are rare. Other authors have reported on the particle-to-particle variability inherent in

395   ground meteorites (Jessberger, et al., 2001); however, the direct comparison presented

396   here allows some clear conclusions to be drawn. The variability displayed here for the

397   Allende meteorite demonstrates the need to characterise samples in detail, since this

398   heterogeneity could have significant consequences when analysing the surface or bulk

399   properties. For example, the rates of catalytic processes or early or late release of an

400   ablating material could be dominated by a statistically uncommon particle or active site.

401   One further observation is that the elemental heterogeneity in Chergach is not significantly

402   different to that in Allende. While the texture of the grains is significantly different, grains of

403   similar elements are present with a similar heterogeneity. This suggests that Chergach and

404   other OC meteorites may be similar to the comparatively rare CC meteorites as IDP

405   analogues.

406   3.3.   Crystal Structure

407   The crystal structure of the analogue used can be important for many applications. It is

408   crucial, for example, when studying the differential ablation of IDPs since each element will

409   be released dependent upon the melting points of its constituent phases and its vapour

410   pressure over these phases. The crystal structure of the analogues was investigated by

411   powder X-Ray Diffraction (XRD, Bruker D8 equipped with a germanium monochromator,

412   using Cu K-α radiation). Measured patterns were compared to literature structures *via* a

413   Rietveld refinement. This involves reproducing a pattern by comparison to one or more

414   structures. Inputs such as the crystallographic space group, lattice parameters and atomic

415   positions allow the prediction of patterns which can be compared to the experimental

416   observations. Factors such as nanocrystallinity and sample displacement can also be

417   simulated to investigate peak shifts and broadening effects. Here this was carried out using

418   the TOPAS software (McCusker, et al., 1999).

3.3.1. Meteoric and Terrestrial Material

419

420 XRD analysis was only performed for the Chergach H5 OC due to the limited availability of
421 other samples. Observed patterns for the albite and peridot olivine samples are compared
422 to that of Chergach in Figure 6. Measured patterns (in black) can be reproduced by Rietveld
423 refinements (in red). For peridot olivine a forsterite structure produces good agreement, for
424 albite a structure of that mineral agrees well, and for Chergach structures of forsterite,
425 albite and ferrosilite combine to give a good representation of the data. Whilst ferrosilite is
426 not likely present in significant quantities, the enstatite end member of the same solid
427 solution series has a similar structure. This suggests that in structural terms Chergach
428 chondrite can be represented simply by a mixture of terrestrial minerals. Comparison to the
429 SEM-EDX mapping, particularly the similarity of the heterogeneous phases present suggests
430 that this can also be extended to other meteorites and IDPs. It is worth noting that the
431 sample likely contains many other minor phases which are below the limits of detection
432 here.

433 In terms of ablation experiments, individual minerals are useful to characterise phase
434 changes as a function of heating (Sandford and Bradley, 1989). Mixtures of minerals may be
435 valuable to compare to meteoritic aggregates or even to IDPs if available, and hence
436 evaluate the effect of grain aggregation and porosity on the release of the elemental
437 constituents. Consideration should be given, however, to the variation of melting points
438 across solid solution series e.g. (Bowen, 1913). In the specific case of the Chergach
439 meteorite (olivine composition $Fo_{81.6}$, (Weisberg, et al., 2008)) the melting point of some
440 phases may be similar, however for a more general study such considerations should be
441 taken into account and terrestrial mineral analogues chosen with care. Terrestrial minerals
442 can also be of great value in calibrating instruments, providing simple systems with known
443 elemental ratios which are easy to characterise and available in greater supply than
444 meteorite samples.

3.3.2. Synthetic samples

445

446 XRD patterns for the synthetic samples discussed in this study are shown in Figure 7.
447 Reitveld refinement (see Section 3.3, above) has a variable, though generally good, ability to
448 reproduce the observed patterns and in some cases providing useful information regarding
449 the synthetic product.

450 $Mg_xFe_{2-x}SiO_4$ materials are mainly amorphous by XRD. In the case of Fe_2SiO_4 the broad
451 crystalline peaks observed can be fitted with a goethite phase. For $MgFeSiO_4$ the similarly
452 broad peaks are compared to a 6 line ferrihydrite phase. Ferrihydrite is a hydrated iron
453 oxide similar to goethite. The broadness of these peaks, particularly that around 35°, is an
454 indication of an amorphous phase or of crystals on the nm scale. For $MgFeSiO_4$ the pattern
455 has been fitted assuming crystallites of 2.5 nm radius and for Fe_2SiO_4 the crystallites are
456 assumed to have radii of 5.2 nm. This nanocrystallinity is discussed further in the context of

457 the particle morphologies in section 3.4. Implications of this crystallinity in terms of using
458 these materials as analogues for MSPs are discussed in section 3.6.

459 For an annealed sample of $MgFeSiO_4$ strong crystalline peaks are observed, which can be
460 fitted with a hematite phase. Repeated SEM-EDX analysis shows that the composition does
461 not change, suggesting that Mg and Si are present as an amorphous or nanocrystalline
462 $MgSiO_3$ phase.

463 The XRD pattern of synthetic goethite is well fitted by assuming a structure of that mineral.
464 Upon annealing a sample of this material at 573 K for 24 hours the XRD pattern could be
465 modelled reasonably well by a hematite structure, consistent with the dehydration of the
466 goethite (Gualtieri and Venturelli, 1999). The fit in this case is imperfect, notably some
467 peaks show significant broadening and the relative peak intensities are not well
468 represented. Since peak broadening due to crystalline size is angle dependent this is likely
469 an indication of relatively small crystallites (perhaps 50-100 nm in radius) but we were not
470 able to find a crystallites size which gave a good fit. Peak intensity variations are likely due
471 to some preferred orientation. Implications of this crystallinity in terms of using these
472 materials as analogues for MSPs are also discussed in section 3.5.

473 **3.4.   Surface Area and Morphology**

474 Surface properties are of paramount importance for the heterogeneous reactivity of an
475 atmospheric solid and therefore an analogue intended to investigate such phenomena. The
476 upper limit to the available reactive surface area was measured for the materials discussed
477 here by the Brunauer, Emmet and Teller (BET, Micrometrics ASAP 2020) method. The results
478 are shown in Table 1. The anomalously high specific surface area for the $Mg_xFe_{2-x}SiO_4$
479 materials is due to their unusual surface morphology.

480 This was investigated by Transmission Electron Microscopy (TEM, FEI Tecnai F20 200kV
481 FEGTEM fitted with a Gatan Orius SC600 CCD camera), with a representative micrograph
482 shown in Figure 8. The thin, folded sheet like nature of the material leads to a large surface
483 potentially being available for uptake and reaction of gases.

484 The inset to Figure 8 shows that at atomic resolution nanocrystalline domains can be seen
485 on the surface of the $MgFeSiO_4$. The scale of these domains is close to the 2.5 nm radius
486 required to resolve the ferrihydrate peaks in the XRD analysis discussed above. This is
487 compelling evidence that these crystalline domains produce the peaks seen in the XRD
488 patterns and can therefore be considered an upper limit to their size. The implications of
489 this nanocrystallinity in terms of using these materials as analogues for MSPs are discussed
490 in section 3.5.

491 The surface area which is actually involved in reaction will depend on the reactivity in a
492 given system, however this large upper limit allows measurement of processes which are
493 relatively slow (Frankland, et al., 2015). The question of available surface area is also
494 pertinent in the environment, since fractal or dendritic particles are often represented as

495 spheres for reasons of computation efficiency (Saunders, et al., 2007). Atmospheric
496 processing by H_2O and acidic gases may also change the available surface area over time.
497 Any use of such materials for surface science should include a careful study of the available
498 surface area. In contrast, crystalline materials such as the goethite and hematite analogues
499 presented here generally have BET surface areas close to that calculated by assuming
500 spherical particles of reasonable size distribution (see Section 3.5). In that case the available
501 surface area in a given experiment can often be well approximated by considering the
502 experimental geometry (e.g. a coated flow tube), or assuming that layered samples of
503 particles are close packed spheres with associated pore spaces (Keyser, et al., 1991).

3.5. Size Distributions and Density

505 The size distribution of an analogue can be important for many reasons. For example, a
506 layered sample of uniform sized particles might be expected to close pack with open pores,
507 whilst a more heterogeneous distribution might have these pores between larger particles
508 filled by smaller particles. Evaporation of particles may be kinetically controlled by the
509 surface for smaller particles, or diffusion through the molten bulk of larger particles. Density
510 is also important in thermal studies since it impacts on the conductivity of the material, and
511 in surface studies since the density of active sites is likely related to the density of a
512 particular surface feature (e.g. a particular ion or structural defect).

513 For dense, approximately spheroidal particles such as the hematite, goethite, enstatite /
514 hematite and ground meteorites and minerals described here measuring the particle size
515 distribution, which results from grinding, is important for designing experiments and
516 interpreting results. For particles on the µm scale, optical microscopy can be used to probe
517 such properties. Here we have used a backlit optical microscope equipped with an objective
518 with a magnification of 10× to image arrays of particles. Typically around 3 dozen images
519 containing 300-600 individual particles were produced using the following algorithm. First,
520 particles were differentiated from the image background by the pixel brightness; second, to
521 account for particles lying on top of each other in the images, the identified particles were
522 artificially eroded until they separate and then rebuilt until they touch; particles in contact
523 with the image edge were discarded; a minimum particle size was set to remove a
524 background of smaller particles from each image; the area of each particle was then
525 calculated (pixels were converted to μm^2 by reference to a standard 1 µm image). Control of
526 the minimum size and pixel brightness threshold allow the analysis to function even for
527 moderately transparent or reflective particles. Each particle area was converted to an
528 equivalent circular radius, and the resulting particle size distribution was then fitted to a log-
529 normal distribution and normalised to a probability density function for comparison.

530 The erosion and reconstruction process introduces several uncertainties into the analysis.
531 First, the volume of a particle which lies on top of another is not counted, giving a
532 downward bias in the estimated size, while imperfect separation of particles where the
533 distance of contact is similar to the particle dimensions leads to an upward bias. Treating

534 particle radius based on area is a major assumption of this method. For example, if the
535 particle contacts a substrate or gas medium in profile then this may be valid, provided that
536 the particles lay similarly *in situ* to their position on the microscope slide. However if volume
537 properties (such as optical extinction) of the material is to be investigated then this method
538 would likely overestimate the volume distribution, since gravitational settling on the surface
539 of the microscope slide will tend to favour the particles laying horizontally. This would result
540 in the shortest dimension being in the vertical (which is neglected here).

541 Example images for two of the meteorites and two of the terrestrial minerals discussed here
542 are shown along with the measured size distributions for the Chergach meteorite in Figure
543 9. Figure 9 (b) shows the result of analysing Figure 9 (a) using the image analysis software,
544 where overlapping particles have been separated and all those which were touching the
545 image edge have been discarded. The sizes of the remaining particles are used in
546 determining the size distributions. These observed distributions have mean sizes within the
547 stated pore size of the sieves used for separation. In general, materials which form
548 needle-like particles (e.g. albite, see Figure 7 d) give slightly larger sizes in this analysis since
549 they are better able to penetrate the pores in the sieves.

550 Size analysis techniques for smaller particles generally involve suspending particles in either
551 a gaseous (e.g. Scanning Mobility Particle Size (SMPS) analysis (Liu and Deshler, 2003)) or
552 liquid (e.g. Dynamic Light Scattering (DLS) (Chu, 2008)) medium. Aggregation can influence
553 the results of these experiments such that in some cases only the limits of particle sizes are
554 measurable. Measurements by both SMPS and DLS have shown that the $Mg_xFe_{2-x}SiO_4$
555 analogues discussed here have primary particle radii on the order of 200-500 nm. TEM
556 imaging shows the presence of some particles on smaller scales (down to 10s of nm).

557 Proper measurement and interpretation of particle sizes is extremely specific to the
558 application in question, however one general point to note is that while generating
559 analogues to IDPs on the appropriate scale is relatively easy, the relatively small size of
560 MSPs (molecular dimensions up to 100 nm radii (Bardeen, et al., 2008)) means that
561 manufacturing analogues for these particles in sufficient quantity for many experiments is
562 extremely challenging. Instead, the approach in the present study is to generate particle
563 analogues likely to have similar properties, and the measured properties (e.g. rates or
564 extinctions) extrapolated to atmospherically relevant particle size distributions.

565 Another volume dependent quantity which can be important for experimental applications
566 is the mass density of the analogue. Mass densities for some of the analogues discussed
567 here are given in Table 1. The synthetic samples have densities significantly lower than for
568 their equivalent bulk minerals, including those materials which are crystalline. This suggests
569 a significant porosity, in agreement with the morphology described above for the
570 $Mg_xFe_{2-x}SiO_4$ materials. Jessberger, et al. (2001) also noted a significant porosity in collected
571 micrometeorites and IDPs.

572 **3.6.   Discussion**

573 The meteorite samples discussed here represent a range of types (CC and OC, differing
574 metamorphic groups). Whilst CC materials such as CI and CM appear to dominate the IDP
575 flux, design of experiments using meteorites as IDP analogues is generally restricted to
576 those types for which large masses of sample are readily available. The elemental
577 composition, heterogeneity and crystal structure data presented indicate, however, that in
578 many cases OC meteorites or even single minerals represent suitable analogues to IDPs
579 (even beyond the 10 % of IDPs which are OC material). Murchison is a good example of an
580 aqueously altered chondrite (groups 2) and contains significant hydrated minerals such as
581 philosylicates, as found in fine grained IDPs (Taylor, et al., 2012). These phases will
582 dehydrate and recrystallise when heated and so will most likely ablate similarly to the
583 feldspathic minerals present in OCs. In addition, analysis of the NWA meteorite shows that
584 there are large deviations within CC meteorites, and that many of these may be useful only
585 for examining extreme or rare cases of IDPs. For example, studies are underway at the
586 University of Leeds into differential ablation using a new Meteor Ablation Simulator (MASI)
587 instrument (Gómez Martín, et al., 2016 - Unpublished results). Kearsley, et al. (2009)
588 produced cometary analogues for impact studies in aerogel and Al foil by aggregating
589 mineral fragments using an acrylic adhesive. These analogues provide excellent insights into
590 the collection of IDPs and cometary dust in aerogel. From the point of view of chemical
591 ablation and surface chemistry studies, which take place on a relatively long time scale
592 compared to impact and where the adhesive may cause undesired interferences, further
593 characterisation experiments are required. The adhesive coating would also be likely to
594 interfere with surface science experiments, where the mineral surface should be exposed to
595 be observed directly.

596 Saunders and Plane (2011) have described a method of producing MSP analogues by
597 photolysis of chemical precursors which then recondense in the gas phase. Amorphous
598 $Mg_xFe_{2-x}SiO_4$ materials and Fe oxides are produced with a primary particle radius of 5-10
599 nm. These small primary particles agglomerate to produce fractal-like particles, likely a good
600 representation of environmental MSPs. These particles have been probed for their optical
601 properties and ice nucleating ability (Saunders, et al., 2010, Saunders and Plane, 2006). We
602 note that the amorphous nature found for those particles is similar to that described here.
603 Where the primary particle radius is 5-10 nm, this sets the upper limit of the crystallite size
604 similar to $Mg_xFe_{2-x}SiO_4$ sheets with maximum thicknesses / domain radii of several nm
605 (Figure 8).

606 One significant difference is that the photochemical methods are able to produce Fe oxides
607 which are amorphous, whereas we only observe crystalline products. This may simply be
608 due to the size of the crystallites formed. Whereas in the photochemistry experiments many
609 particles nucleate, take up the available precursor and at some point grow faster by
610 agglomeration than deposition to existing particles, our solution phase synthesis allows
611 relatively fewer particles to grow to larger sizes at which their crystallinity is measurable.

612 Since MSP remain at small sizes, the photochemical method is likely more representative, so
613 that care should be taken when using the materials synthesised by sol-gel processes as
614 analogues for MSP.

615 Biermann, et al. (1996), who used micrometeorites as analogues for MSP nucleating
616 crystallisation in polar stratospheric clouds, found that nucleation rates were not high
617 enough to explain observed cloud. As the authors in that study observed, micrometeorites
618 are generally compact, dense particles coated with magnetite crystals. MSPs which are
619 present in stratospheric droplets, on the other hand, will have been processed and largely
620 dissolved by the acidic content of those droplets (Saunders, et al., 2012). Murphy, et al.
621 (2014) used single particle mass spectrometer measurements to show that silicon and
622 aluminium in such droplets are generally solid while most other metals are in solution. A
623 silica or alumina substrate would therefore seem more appropriate for investigating
624 nucleation in polar stratospheric clouds.

625 Nachbar, et al. (2016) used photolysis of chemical precursors to produce very small (several
626 nm radii) particles, which were held in an ion trap at supersaturated conditions and used to
627 measure nucleation kinetics and particle growth. These particles are alike both in size and
628 composition to MSPs and therefore are highly appropriate as MSP analogues. As with the
629 photochemical technique of Saunders and Plane (2011), the difficulty in using this material
630 to investigate a wider range of applications lies in producing bulk amounts (typically several
631 grams are required for uptake experiments).

632 **4. Conclusions**

633 This study has demonstrated the preparation of a variety of analogues for IDPs and MSPs.
634 The methods are fairly straightforward to implement and use materials which are widely
635 available. No single analogue best represents IDPs or MSPs in general since this rather
636 depends on the application being investigated. Instead some common issues are raised in
637 order to help researchers choose materials for a wide range of applications.

638 It has been shown that reasonable analogues for IDPs can be produced by grinding and size
639 segregating meteoritic material. The elemental composition of such analogues will vary
640 slightly from the target material but phases which are present in IDPs will be well
641 represented in ground meteorites. OCs are scarce in micrometeorite collections, but
642 samples of OC meteorites are much easier to source than CCs. Although ground OCs
643 produce denser, more compact analogues, elemental compositions and mineralogy are
644 reasonably close to those of average IDPs. Terrestrial materials such as peridot olivine,
645 labradorite, anorthite and albite, when similarly ground, are good analogues for individual
646 phases within IDPs, particularly for applications such as instrument calibration where
647 paucity of sample can be an issue. In the cases of both meteorites and terrestrial minerals it
648 was shown that mechanical sieving can reliably produce target particle size fractions which
649 are representative of IDPs.

650 Chemical syntheses were presented for compounds with elemental compositions similar to
651 the olivine solid solution series. These are thought to be nanocrystalline folded sheets. Such
652 a morphology is not likely representative of MSPs or IDPs, however it should be noted that
653 the domain size of such crystallites is similar to the primary particle size of MSPs and
654 therefor a similar nanocrystallinity may be possible. The large surface area presented by this
655 morphology allows measurement of relatively unreactive processes which occur at the
656 interface, whilst the elemental composition is similar to that expected for MSPs. These
657 materials can be annealed to produce enstatite and hematite, which are also suitable
658 analogues for potential components of MSPs.

659 A chemical synthesis was also presented for crystalline goethite, which could be dehydrated
660 to produce hematite. Goethite is a potential component of MSP whilst hematite could be
661 present in both IDPs and MSPs. The crystalline nature of these materials may not be
662 representative of MSPs; nevertheless for some applications they may still be considered
663 suitable analogues.

664 Finally, it is clearly of great importance that in laboratory experiments where analogues are
665 used for IDP or MSP materials, careful attention is paid to characterising the analogue and
666 ensuring that the limitations of its applicability are understood.

667

676

677 **References**

678 Ade, P.A.R., et al., 2014. Planck 2013 results. XIV. Zodiacal emission. A&A 571, A14.

679 Bardeen, C.G., Toon, O.B., Jensen, E.J., Marsh, D.R., Harvey, V.L., 2008. Numerical
680 simulations of the three-dimensional distribution of meteoric dust in the mesosphere and
681 upper stratosphere. J. Geophys. Res.: Atmos. 113 (D17), D17202.

682 Biermann, U.M., Presper, T., Koop, T., Mößinger, J., Crutzen, P.J., Peter, T., 1996. The
683 unsuitability of meteoritic and other nuclei for polar stratospheric cloud freezing. Geophys.
684 Res. Lett. 23 (13), 1693-1696.

685 Bigg, E.K., 2012. Sources of insoluble inclusions in stratospheric sulfate particles. Meteorit.
686 Planet. Sci. 47 (5), 799-805.

687 Blanchard, M.B., Brownlee, D.E., Bunch, T.E., Hodge, P.W., Kyte, F.T., 1980. Meteoroid
688 ablation spheres from deep-sea sediments. Earth Plan. Sci. Lett. 46 (2), 178-190.

689 Bowen, N.L., 1913. The melting phenomena of the plagioclase feldspars. Amer. J. Sci. (210),
690 577-599.

691 Burchell, M.J., Mann, J., Creighton, J.A., Kearsley, A.T., Graham, G., Franchi, I.A., 2006.
692 Identification of minerals and meteoritic materials via Raman techniques after capture in
693 hypervelocity impacts on aerogel. Meteorit. Planet. Sci. 41 (2), 217-232.

694 Burgess, R., Wright, I.P., Pillinger, C.T., 1991. Determination of sulphur-bearing components
695 in C1 and C2 carbonaceous chondrites by stepped combustion. Meteoritics 26 (1), 55-64.

696 Carrillo-Sánchez, J.D., Plane, J.M.C., Feng, W., Nesvorný, D., Janches, D., 2015. On the size
697 and velocity distribution of cosmic dust particles entering the atmosphere. Geophys. Res.
698 Lett. 42 (15), 6518-6525.

699 Chu, B., 2008. Dynamic light scattering. In: Borsali, R., Pecora, R. (Eds.), Soft matter
700 characterization. 335-372. Springer Netherlands.

701 Clarke, R., Jarosevich, E., Mason, B., Nelen, J., Gomez, M., Hyde, J.R., 1971. The Allende,
702 Mexico, Meteoroite Shower. Smithsonian Institution Press, Washington.

703 Consolmagno, G.J., Britt, D.T., Macke, R.J., 2008. The significance of meteorite density and
704 porosity. Chem. der Erde - Geochem. 68 (1), 1-29.

705 Court, R.W., Sephton, M.A., 2011. The contribution of sulphur dioxide from ablating
706 micrometeorites to the atmospheres of Earth and Mars. Geochim. Cosmochim. Acta 75 (7),
707 1704-1717.

708 Dobrică, E., Engrand, C., Duprat, J., Gounelle, M., Leroux, H., Quirico, E., Rouzaud, J.N., 2009.
709 Connection between micrometeorites and Wild 2 particles: From Antarctic snow to
710 cometary ices. Meteorit. Planet. Sci. 44 (10), 1643-1661.

711 Farlow, N.H., Ferry, G.V., Blanchard, M.B., 1970. Examination of surfaces exposed to a
712 noctilucent cloud, August 1, 1968. J. Geophys. Res. 75 (33), 6736-6750.

713 Fixsen, D.J., Dwek, E., 2002. The zodiacal emission spectrum as determined by COBE and its
714 implications. Astrophys. J. 578 (2), 1009.

715 Frank, D.R., Zolensky, M.E., Le, L., 2014. Olivine in terminal particles of Stardust aerogel
716 tracks and analogous grains in chondrite matrix. Geochim. Cosmochim. Acta 142, 240-259.

717 Frankland, V.L., James, A.D., Feng, W., Plane, J.M.C., 2015. The uptake of HNO_3 on meteoric
718 smoke analogues. J. Atmos. Sol.-Terr. Phys. 127, 150-160.

719 Frankland, V.L.F., James, A.D., Carrillo-Sánchez, J.D., Mangan, T.P., Willacy, K., Poppe, A.R.,
720 Plane, J.M.C., 2016 - in press. Uptake of acetylene on cosmic dust and production of
721 benzene in Titan's atmosphere. Icarus.

722 Frankland, V.L.F., James, A.D., Carrillo-Sánchez, J.D., Nesvorný, D., Plane, J.M.C., 2016 -
723 Unpublised results. CO oxidation on meteoric material with applications to the Venusian
724 lower atmosphere.

725 Fuchs, L.H., Jensen, K.J., Olsen, E.J., 1973. Mineralogy, mineral-chemistry, and composition
726 of the Murchison (C2) meteorite. Smithsonian Institution Press.

727 Gómez Martín, J.C., Bones, D.L., Carrillo-Sánchez, J.D., James, A.D., Trigo-Rodríguez, J.M.,
728 Fegley Jr., B., Plane, J.M.C., 2016 - Unpublished results. Novel experimental simulations of
729 the atmospheric injection of meteoric metals.

730 Greshake, A., KlÖCk, W., Arndt, P., Maetz, M., Flynn, G.J., Bajt, S., Bischoff, A., 1998. Heating
731 experiments simulating atmospheric entry heating of micrometeorites: Clues to their parent
732 body sources. Meteorit. Planet. Sci. 33 (2), 267-290.

733 Gualtieri, A.F., Venturelli, P., 1999. In situ study of the goethite-hematite phase
734 transformation by real time synchrotron powder diffraction, 895.

735 Hedin, J., et al., 2014. The MAGIC meteoric smoke particle sampler. J. Atmos. Sol.-Terr. Phys.
736 118, Part B, 127-144.

737 Hervig, M.E., Deaver, L.E., Bardeen, C.G., Russell Iii, J.M., Bailey, S.M., Gordley, L.L., 2012.
738 The content and composition of meteoric smoke in mesospheric ice particles from SOFIE
739 observations. J. Atmos. Sol.-Terr. Phys. 84–85, 1-6.

740 Hervig, M.E., Gordley, L.L., Deaver, L.E., Siskind, D.E., Stevens, M.H., Russell, J.M., Bailey,
741 S.M., Megner, L., Bardeen, C.G., 2009. First satellite observations of meteoric smoke in the
742 middle atmosphere. Geophys. Res. Lett. 36 (18), L18805.

743 Hilchenbach, M., et al., 2016. Comet 67P/Churyumov–Gerasimenko: Close-up on Dust
744 Particle Fragments. Astrophys. J. Lett. 816 (2), L32.

745 Hörz, F., et al., 2006. Impact features on Stardust: Implications for comet 81P/Wild 2 dust.
746 Science 314 (5806), 1716-1719.

747 Hörz, F., Zolensky, M.E., Bernhard, R.P., See, T.H., Warren, J.L., 2000. Impact features and
748 projectile residues in aerogel exposed on Mir. Icarus 147 (2), 559-579.

749 Hoyle, C.R., Engel, I., Luo, B.P., Pitts, M.C., Poole, L.R., Grooß, J.U., Peter, T., 2013.
750 Heterogeneous formation of polar stratospheric clouds – Part 1: Nucleation of nitric acid
751 trihydrate (NAT). Atmos. Chem. Phys. 13 (18), 9577-9595.

752 Hunten, D.M., Turco, R.P., Toon, O.B., 1980. Smoke and dust particles of meteoric origin in
753 the mesosphere and stratosphere. J. Atmos. Sci. 37 (6), 1342-1357.

754 Hutchison, R., 2004. Meteorites: A petrologic, chemical and isotopic synthesis. Cambridge
755 University Press.

756 James, A.D., Moon, D.R., Feng, W., Lakey, P.S.J., Frankland, V.L.F., Heard, D.E., Plane, J.M.C.,
757 2016 - Unpublished results. The uptake of HO_2 on meteoric smoke analogues.

758 Janches, D., Dyrud, L.P., Broadley, S.L., Plane, J.M.C., 2009. First observation of
759 micrometeoroid differential ablation in the atmosphere. Geophys. Res. Lett. 36 (6), L06101.

760 Jessberger, E.K., Stephan, T., Rost, D., Arndt, P., Maetz, M., Stadermann, F.J., Brownlee, D.E.,
761 Bradley, J.P., Kurat, G., 2001. Properties of interplanetary dust: information from collected
762 samples. In: Grün, E., Gustafson, B.Å.S., Dermott, S., Fechtig, H. (Eds.), Interplanetary Dust.
763 253-294. Springer Berlin Heidelberg.

764 Kearsley, A.T., Burchell, M.J., Price, M.C., Graham, G.A., Wozniakiewicz, P.J., Cole, M.J.,
765 Foster, N.J., Teslich, N., 2009. Interpretation of Wild 2 dust fine structure: Comparison of
766 Stardust aluminum foil craters to the three-dimensional shape of experimental impacts by

767   artificial aggregate particles and meteorite powders. Meteorit. Planet. Sci. 44 (10), 1489-
768   1509.

769   Keyser, L.F., Moore, S.B., Leu, M.T., 1991. Surface reaction and pore diffusion in flow-tube
770   reactors. J. Phys. Chem. 95 (14), 5496-5502.

771   Kohout, T., et al., 2014. Density, porosity and magnetic susceptibility of the Košice meteorite
772   shower and homogeneity of its parent meteoroid. Planet. Space Sci. 93–94, 96-100.

773   Lisse, C.M., et al., 2006. Spitzer spectral observations of the deep impact ejecta. Science 313
774   (5787), 635-640.

775   Liu, P.S.K., Deshler, T., 2003. Causes of concentration differences between a scanning
776   mobility particle sizer and a condensation particle counter. Aerosol Sci. Tech. 37 (11), 916-
777   923.

778   Love, S.G., Brownlee, D.E., 1993. A direct measurement of the terrestrial mass accretion rate
779   of cosmic dust. Science 262 (5133), 550-553.

780   Maurette, M., Jehanno, C., Robin, E., Hammer, C., 1987. Characteristics and mass
781   distribution of extraterrestrial dust from the Greenland ice cap. Nature 328, 699 - 702.

782   McCusker, L.B., Von Dreele, R.B., Cox, D.E., Louer, D., Scardi, P., 1999. Rietveld refinement
783   guidelines. J. Appl. Cryst. 32 (1), 36-50.

784   Murphy, D.M., Froyd, K.D., Schwarz, J.P., Wilson, J.C., 2014. Observations of the chemical
785   composition of stratospheric aerosol particles. Quart. J. Royal Met. Soc. 140 (681), 1269-
786   1278.

787   Nachbar, M., Duft, D., Mangan, T.P., Gomez Martin, J.C., Plane, J.M.C., Leisner, T., 2016.
788   Laboratory measurements of heterogeneous CO_2 ice nucleation on nanoparticles under
789   conditions relevant to the Martian mesosphere. J. Geophys. Res.: Plan. (121), e004978.

790   Neely, R.R., English, J.M., Toon, O.B., Solomon, S., Mills, M., Thayer, J.P., 2011. Implications
791   of extinction due to meteoritic smoke in the upper stratosphere. Geophys. Res. Lett. 38 (24),
792   L24808.

793   Nesvorný, D., Janches, D., Vokrouhlický, D., Pokorný, D., Bottke, W.F., Jenniskens, P., 2011.
794   Dynamical model for the zodiacal cloud and sporadic meteors. Astrophys. J. 743 (2), 129.

795   Nesvorný, D., Jenniskens, P., Levison, H.F., Bottke, W.F., Vokrouhlický, D., Gounelle, M.,
796   2010. Cometary origin of the zodiacal cloud and carbonaceous micrometeorites.
797   Implications for hot debris disks. Astrophys. J. 713 (2), 816.

798   Opeil Sj, C.P., Consolmagno Sj, G.J., Safarik, D.J., Britt, D.T., 2012. Stony meteorite thermal
799   properties and their relationship with meteorite chemical and physical states. Meteorit. &
800   Planet. Sci. 47 (3), 319-329.

801   Petrie, S., 2004. Products of meteoric metal ion chemistry within planetary atmospheres. 1.
802   Mg^+ at Titan. Icarus 171 (1), 199-209.

803   Plane, J.M.C., 2003. Atmospheric chemistry of meteoric metals. Chem. Rev. 103 (12), 4963-
804   4984.

805   Plane, J.M.C., 2011. On the role of metal silicate molecules as ice nuclei. J. Atmos. Sol.-Terr.
806   Phys. 73 (14–15), 2192-2200.

807 Plane, J.M.C., 2012. Cosmic dust in the earth's atmosphere. Chem. Soc. Rev. 41 (19), 6507-
808 6518.

809 Plane, J.M.C., Feng, W., Dawkins, E.C.M., 2015. The mesosphere and metals: chemistry and
810 changes. Chem. Rev. 115 (10), 4497-4541.

811 Plane, J.M.C., et al., 2014. A combined rocket-borne and ground-based study of the sodium
812 layer and charged dust in the upper mesosphere. J. Atmos. and Sol.Terr. Phys. 118, Part B,
813 151-160.

814 Rapp, M., Plane, J.M.C., Strelnikov, B., Stober, G., Ernst, S., Hedin, J., Friedrich, M., Hoppe,
815 U.P., 2012. In situ observations of meteor smoke particles (MSP) during the Geminids 2010:
816 constraints on MSP size, work function and composition. Ann. Geophys. 30 (12), 1661-1673.

817 Rietmeijer, F.J.M., 2000. Interrelationships among meteoric metals, meteors, interplanetary
818 dust, micrometeorites, and meteorites. Meteorit. Planet. Sci. 35 (5), 1025-1041.

819 Robertson, S., Dickson, S., Horányi, M., Sternovsky, Z., Friedrich, M., Janches, D., Megner, L.,
820 Williams, B., 2014. Detection of meteoric smoke particles in the mesosphere by a rocket-
821 borne mass spectrometer. J. Atmos. Sol.-Terr. Phys. 118, Part B, 161-179.

822 Russell, J.M.I., et al., 2009. The Aeronomy of Ice in the Mesosphere (AIM) mission: Overview
823 and early science results. J. Atmos. Sol.-Terr. Phys. 71 (3–4), 289-299.

824 Sandford, S.A., Bradley, J.P., 1989. Interplanetary dust particles collected in the
825 stratosphere: Observations of atmospheric heating and constraints on their
826 interrelationship and sources. Icarus 82 (1), 146-166.

827 Saunders, R.W., Dhomse, S., Tian, W.S., Chipperfield, M.P., Plane, J.M.C., 2012. Interactions
828 of meteoric smoke particles with sulfuric acid in the Earth's stratosphere. Atmos. Chem.
829 Phys. 12 (10), 4387-4398.

830 Saunders, R.W., Forster, P.M., Plane, J.M.C., 2007. Potential climatic effects of meteoric
831 smoke in the Earth's paleo-atmosphere. Geophys. Res. Lett. 34 (16), L16801.

832 Saunders, R.W., et al., 2010. An aerosol chamber investigation of the heterogeneous ice
833 nucleating potential of refractory nanoparticles. Atmos. Chem. Phys. 10 (3), 1227-1247.

834 Saunders, R.W., Plane, J.M.C., 2006. A laboratory study of meteor smoke analogues:
835 Composition, optical properties and growth kinetics. J. Atmos. Sol.-Terr. Phys. 68 (18), 2182-
836 2202.

837 Saunders, R.W., Plane, J.M.C., 2011. A photo-chemical method for the production of olivine
838 nanoparticles as cosmic dust analogues. Icarus 212 (1), 373-382.

839 Schulz, R., et al., 2015. Comet 67P/Churyumov-Gerasimenko sheds dust coat accumulated
840 over the past four years. Nature 518 (7538), 216-218.

841 Sorensen, C., 2001. Light scattering by fractal aggregates: a review. Aerosol Sci. Tech. 35 (2),
842 648-687.

843 Stephan, T., Flynn, G.J., Sandford, S.A., Zolensky, M.E., 2008. TOF-SIMS analysis of cometary
844 particles extracted from Stardust aerogel. Meteorit. Planet. Sci. 43 (1-2), 285-298.

845 Taylor, S., Lever, J.H., Harvey, R.P., 1998. Accretion rate of cosmic spherules measured at the
846 South Pole. Nature 392 (6679), 899-903.

847   Taylor, S., Matrajt, G., Guan, Y., 2012. Fine-grained precursors dominate the micrometeorite
848   flux. Meteorit. Planet. Sci. 47 (4), 550-564.

849   Toppani, A., Libourel, G., Engrand, C., Maurette, M., 2001. Experimental simulation of
850   atmospheric entry of micrometeorites. Meteorit. Planet. Sci. 36 (10), 1377-1396.

851   Trigo-Rodríguez, J.M., Llorca, J., 2007. On the sodium overabundance in cometary
852   meteoroids. Adv. Space Res. 39 (4), 517-525.

853   Turco, R.P., Toon, O.B., Hamill, P., Whitten, R.C., 1981. Effects of meteoric debris on
854   stratospheric aerosols and gases. J. Geophys. Res.: Oc. 86 (C2), 1113-1128.

855   Vondrak, T., Plane, J.M.C., Broadley, S., Janches, D., 2008. A chemical model of meteoric
856   ablation. Atmos. Chem. Phys. 8 (23), 7015-7031.

857   Weisberg, M.K., Smith, C., Benedix, G., Folco, L., Righter, K., Zipfel, J., Yamaguchi, A.,
858   Aoudjehane, H.C., 2008. The Meteoritical Bulletin, No. 94, September 2008. Meteorit.
859   Planet. Sci. 43 (9), 1551-1584.

860   Weisberg, M.K., Smith, C., Benedix, G., Herd, C.D.K., Righter, K., Haack, H., Yamaguchi, A.,
861   Aoudjehane, H.C., Grossman, J.N., 2009. The Meteoritical Bulletin, No. 96, September 2009.
862   Meteorit. Planet. Sci. 44 (9), 1355-1397.

863   Whalley, C.L., Plane, J.M.C., 2010. Meteoric ion layers in the Martian atmosphere. Faraday
864   disc. 147, 349-368.

865   Witt, G., Hemenway, C.L., Lange, N., Modin, S., Soberman, R.K., 1964. Composition analysis
866   of particles from noctilucent clouds. Tellus 16 (1), 103-109.

867   Zolensky, M.E., Lindstrom, D., 1992. Mineralogy of 12 large "chondritic" interplanetary dust
868   particles, 161-169.

869

870   **Tables**

871

Table 1. Genesis, proposed analogue use, BET surface area and bulk density of samples described in this study.

Analogue	Genesis	Analogue for	BET surface area / $m^2\ g^{-1}$	Mass density / $g\ cm^{-3}$
Mg_2SiO_4	$MgCl_2 + Na_4SiO_4$	MSPs	102 ± 5	
$MgFeSiO_4$	$Fe(SO_4)_2(NH_4)_2 + MgCl_2 + Na_4SiO_4$	MSPs	358 ± 16	2.647 ± 0.004
Enstatite / Hematite	From $MgFeSiO_4$ as above, sintered at 1273 K for 24 hours	MSPs	3.07 ± 0.03	
Fe_2SiO_4	$Fe(SO_4)_2(NH_4)_2 + Na_4SiO_4$	MSPs	244 ± 2	3.2638 ± 0.0007
Goethite	$Fe(SO_4)_2(NH_4)_2 + NaOH$ + compressed air	MSPs	41.4 ± 0.4	3.964 ± 0.006
Hematite	From Goethite as above, dehydrated at 573 K for 24 hours	MSPs	34.4 ± 0.2	
Peridot Olivine*	Skarvebergbukren, Norway N/62	IDPs	n/a	
Albite*	Almeklovdalen, Norway N/37	IDPs	n/a	
Labradorite*	University of Leeds research collection	IDPs	n/a	
Anorthite*	Japan via. Gregory, Botley & co., Chelsea	IDPs	n/a	
Chergach Meteorite	Meteorites-for-sale.com	IDPs	n/a	3.5†
Allende Meteorite	Institute of Space Sciences (CSIC-IECC) research collection	IDPs	n/a	2.9†
Murchison Meteorite	Institute of Space Sciences (CSIC-IECC) research collection	IDPs	n/a	2.9†
NWA 5515 Meteorite	Meteorites-for-sale.com	IDPs	n/a	2.7†

* Terrestrial mineral samples were obtained from the University of Leeds, School of Earth and Environment research collections

†Values from the literature. NWA from Opeil Sj, et al. (2012), others as referenced in Section 2.1

Article reference: ATP4657

Figure Captions

Figure 1. Elemental compositions, normalised to Si, comparing each of the meteorites used here to the composition of CI, CM and its own group (Hutchison, 2004). a) Two size fractions (<19 μm and >177.5 μm) of the Chergach (H5) meteorite. b) The Allende (CV3) and Merchison (CM2) meteorites. c) The North West Africa 5515 (CK4) meteorite, 125-177.5 μm size fraction. Error bars show the 95% confidence interval of 4-8 measurements. Measurement techniques vary, see text for details.

Figure 2. SEM-EDX mapping for a particle of the Chergach meteorite. Si is omitted due to interference from the substrate. The bulk Fo_{82} olivine is clearly shown in the Mg panel. Grains containing Fe & Ca (lower centre), Na & K (lower right and centre right), and each of those elements individually.

Figure 3. Backscatter electron image of a thin section of the Allende meteorite before grinding demonstrating the scale of individual features such as a barred olivine chondrule (A), a porphyritic olivine chondrule (B), the fine grained carbonaceous matrix (C) and a metal sulfide inclusion (D).

Figure 4. SEM-EDX mapping for a particle of the Allende meteorite, showing both a fine aggregate and scoreacious grains. The fine aggregate particle has a higher S content and is more heterogeneous than the scoreacious grain.

Figure 5. SEM-EDX mapping for two particles of the Allende meteorite, showing one single mineral particle and one fine aggregate grain. Si can be included here since a Cu substrate was used. The single mineral (left) particle shows a homogeneous composition consistent with nepheline or sodelite, whilst the fine grain aggregate appears to have an olivine matrix containing grains of diverse composition.

Figure 6. Observed powder X-ray diffraction patterns for peridot olivine, albite and the Chergach meteorite. The black lines show measured data and the red lines show Rietveld refinements. Peridot olivine is compared to a forsterite structure, Albite to a structure of that material and the Chergach meteorite to a combination of both.

Figure 7. XRD patterns for synthetic samples produced in this study. Measured data are in black and fits from Rietveld refinement in red. Data have been scaled and offset to show an appropriate scale in each case.

Figure 8. Typical transmission electron microscope image of the $MgFeSiO_4$ described in this study showing 'folded sheet like' morphology. Insert shows an example of nanocrystalline domains on the sheet surface.
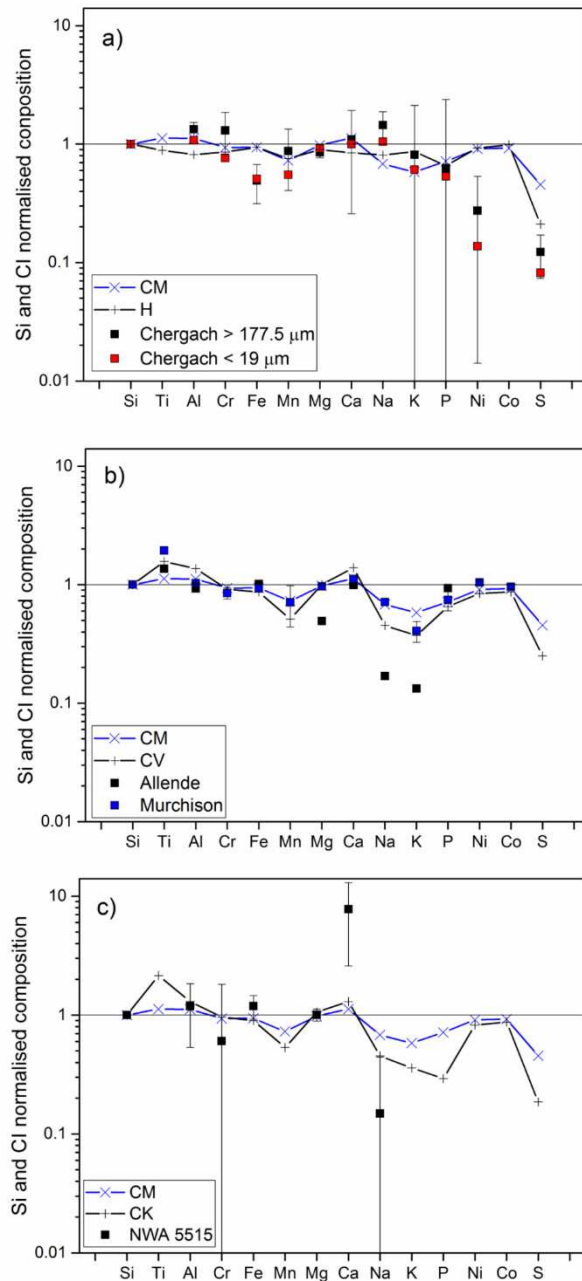
Figure 9. Example microscope images of the 75-125 μm radius fraction for (a) the Chergach meteorite, (c) the Allende meteorite (d) the peridot olivine and (e) the albite samples. Scales for other images are as for the Chergach sample. Panel (b) shows the particles found by the

image analysis software (described in section 3.5) in panel (a). Panel (f) shows a comparison of the measured probability density functions for each of the Chergach size bins investigated.
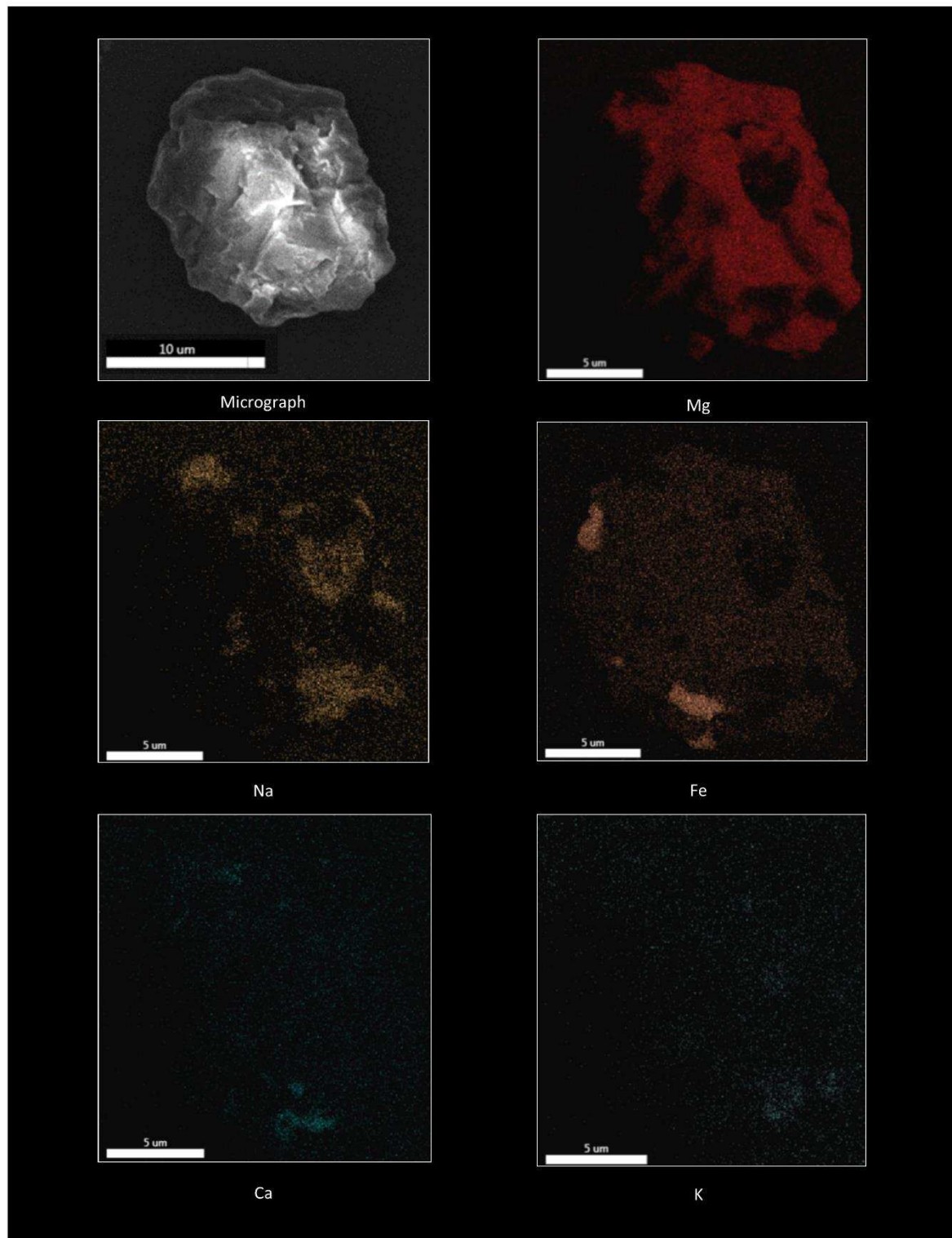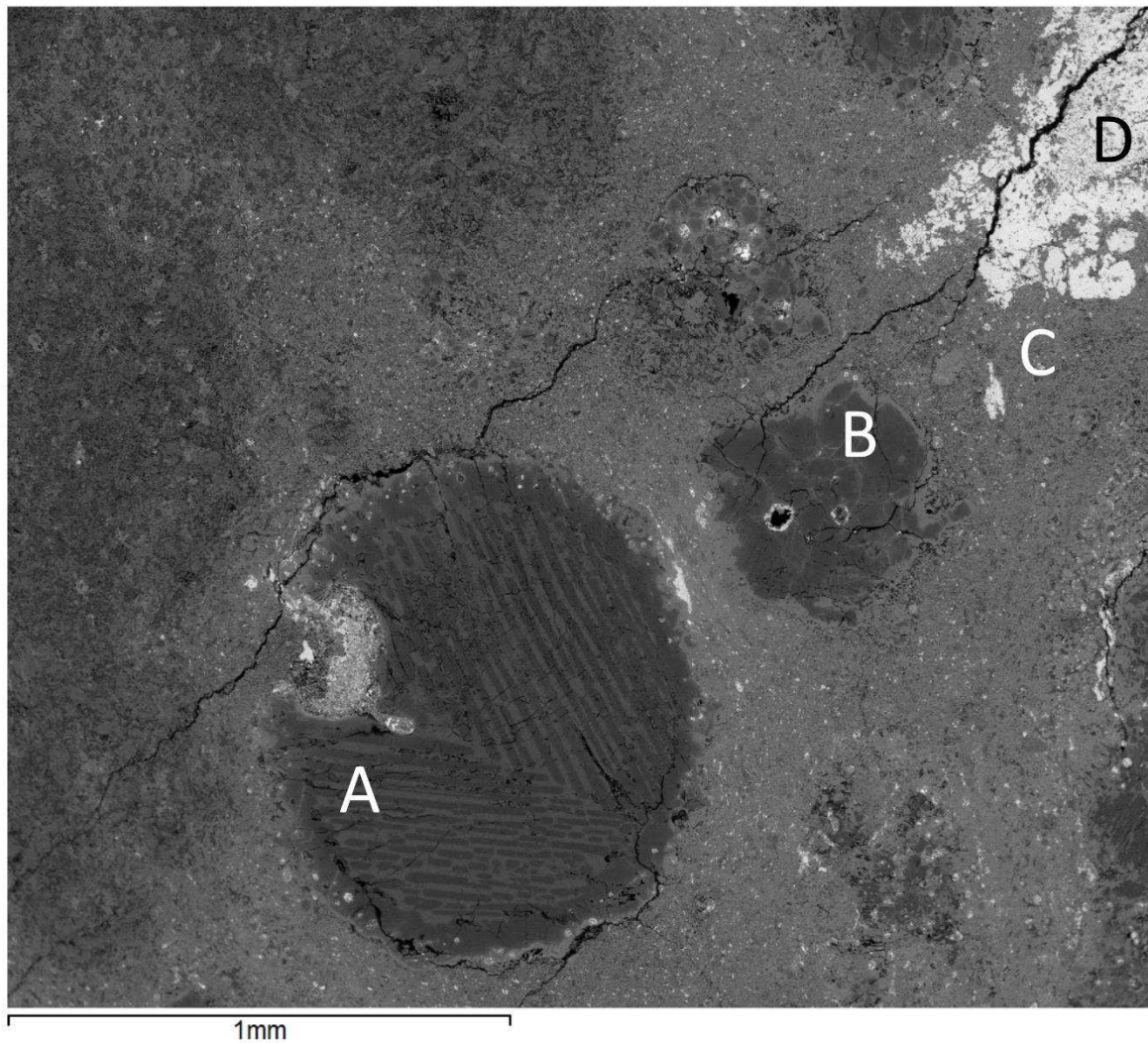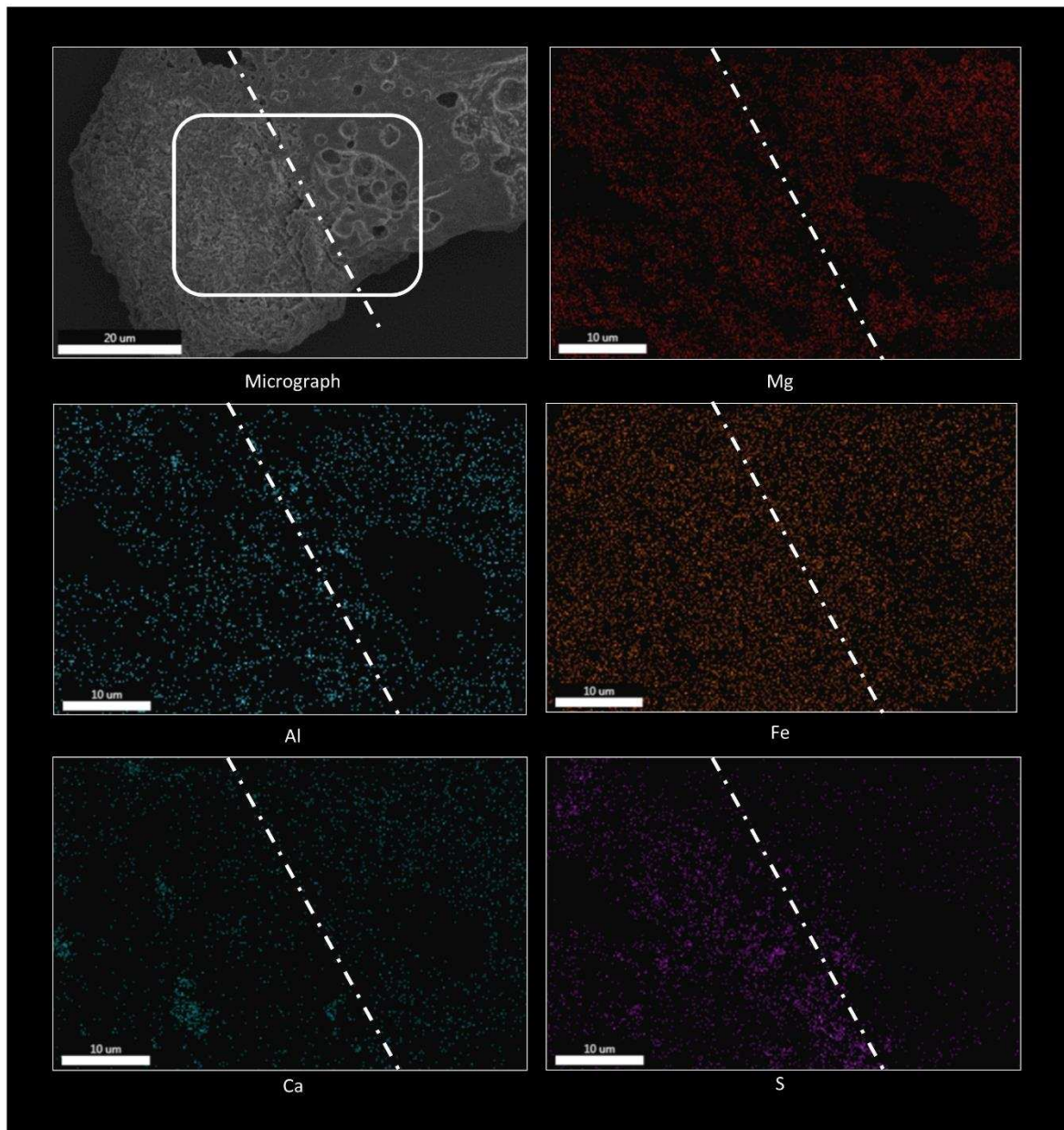
Figures

Figure 1.

Elemental compositions, normalised to Si, comparing each of the meteorites used here to the composition of CI, CM and its own group (Hutchison, 2004). a) Two size fractions (<19 μm and >177.5 μm) of the Chergach (H5) meteorite. b) The Allende (CV3) and Merchison (CM2) meteorites. c) The North West Africa 5515 (CK4) meteorite, 125-177.5 μm size fraction. Error bars show the 95% confidence interval of 4-8 measurements. Measurement techniques vary, see text for details.

Figure 2.

SEM-EDX mapping for a particle of the Chergach meteorite. Si is omitted due to interference from the substrate. The bulk Fo_{82} olivine is clearly shown in the Mg panel. Grains containing Fe & Ca (lower centre), Na & K (lower right and centre right), and each of those elements individually.
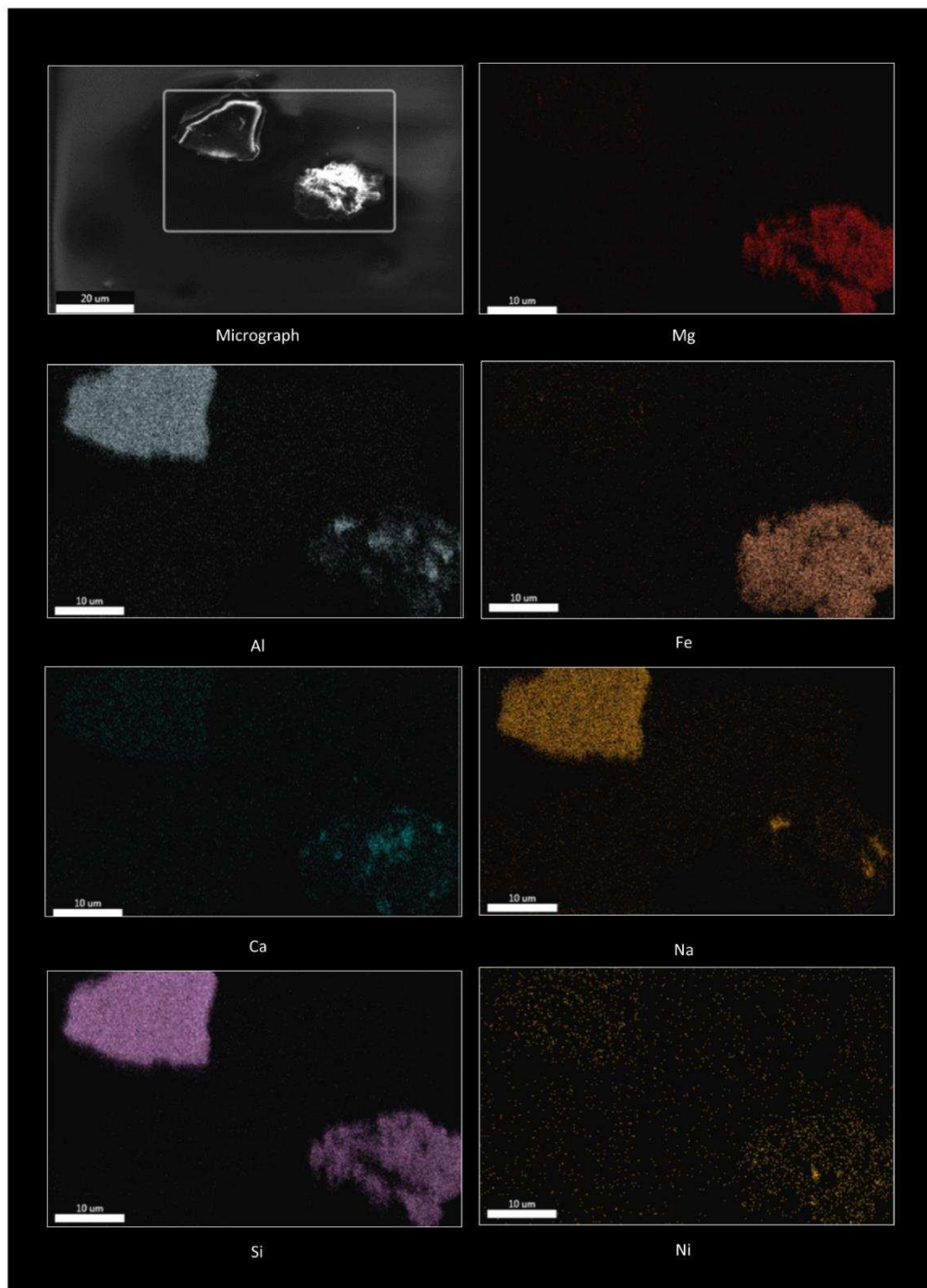
Figure 3.

Backscatter electron image of a thin section of the Allende meteorite before grinding demonstrating the scale of individual features such as a barred olivine chondrule (A), a porphyritic olivine chondrule (B), the fine grained carbonaceous matrix (C) and a metal sulfide inclusion (D).
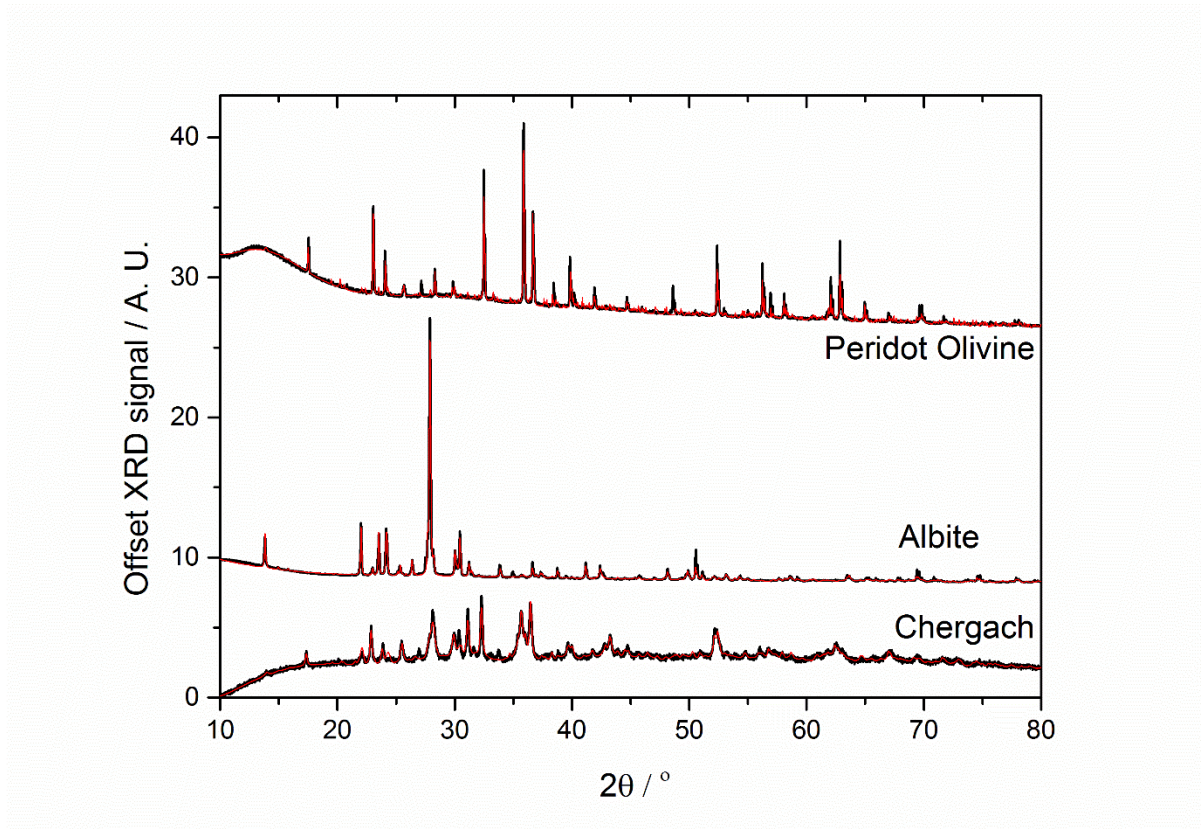
Figure 4.

SEM-EDX mapping for a particle of the Allende meteorite, showing both a fine aggregate and scoreacious grains. The fine aggregate particle has a higher S content and is more heterogeneous than the scoreacious grain.
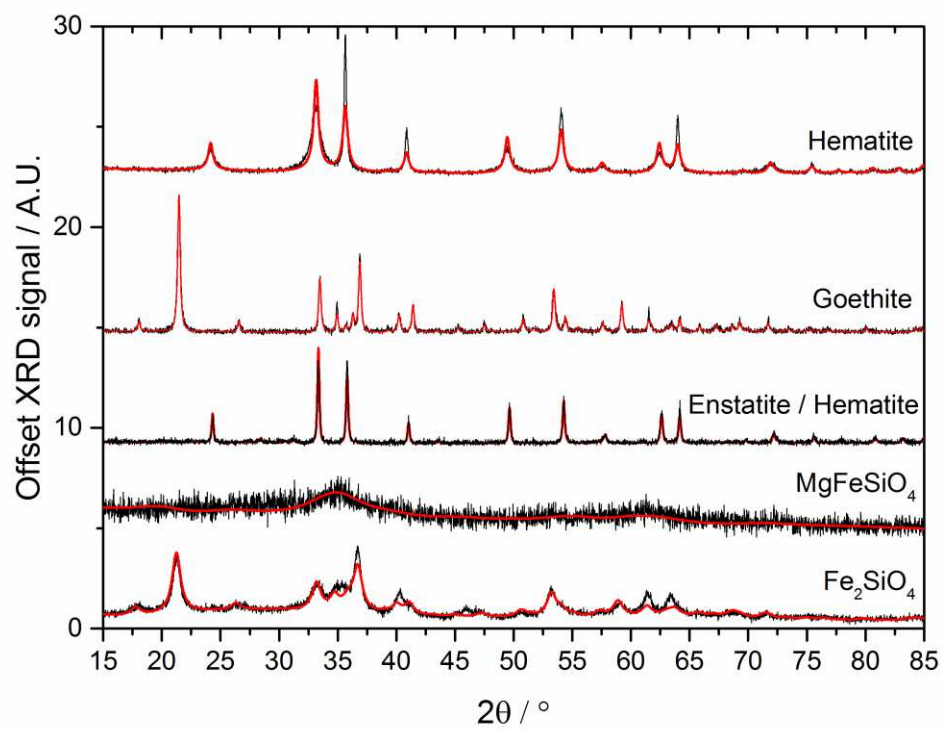
Figure 5.

SEM-EDX mapping for two particles of the Allende meteorite, showing one single mineral particle and one fine aggregate grain. Si can be included here since a Cu substrate was used. The single mineral (left) particle shows a homogeneous composition consistent with nepheline or sodelite, whilst the fine grain aggregate appears to have an olivine matrix containing grains of diverse composition.
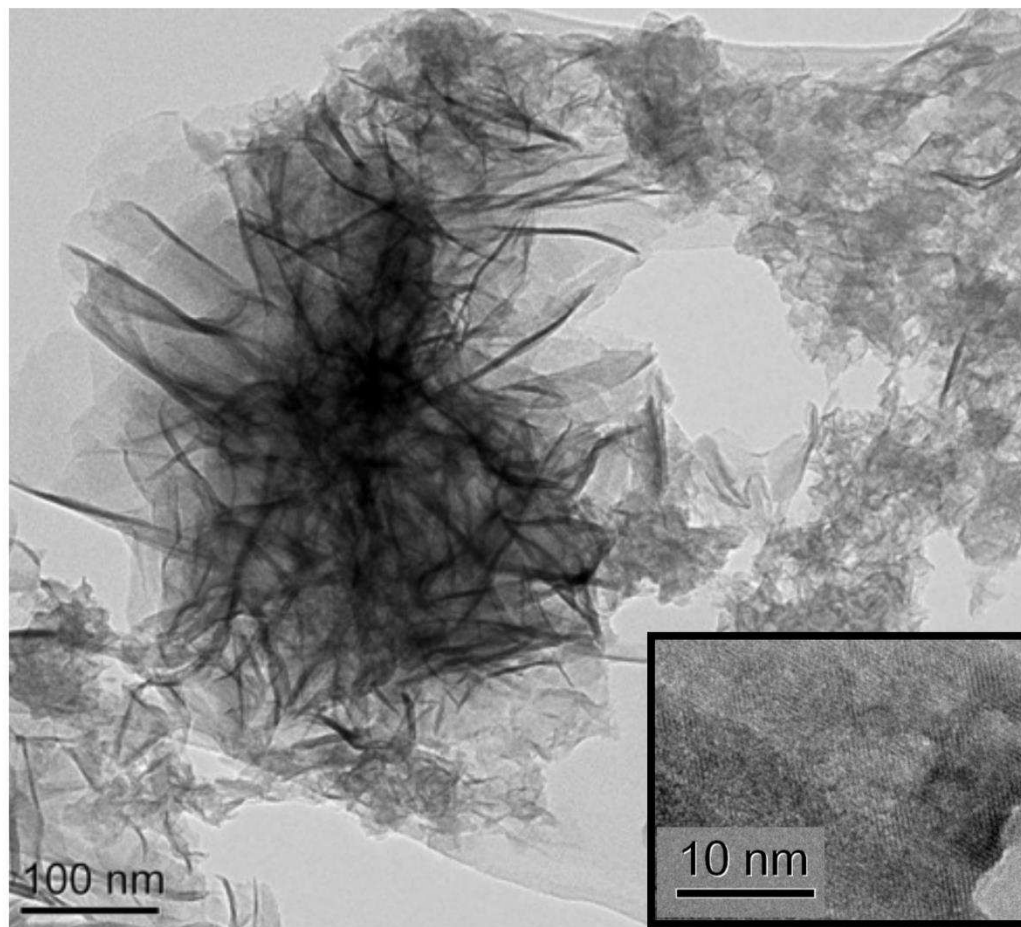
Figure 6.

Observed powder X-ray diffraction patterns for peridot olivine, albite and the Chergach meteorite. The black lines show measured data and the red lines show Rietveld refinements. Peridot olivine is compared to a forsterite structure, Albite to a structure of that material and the Chergach meteorite to a combination of both.
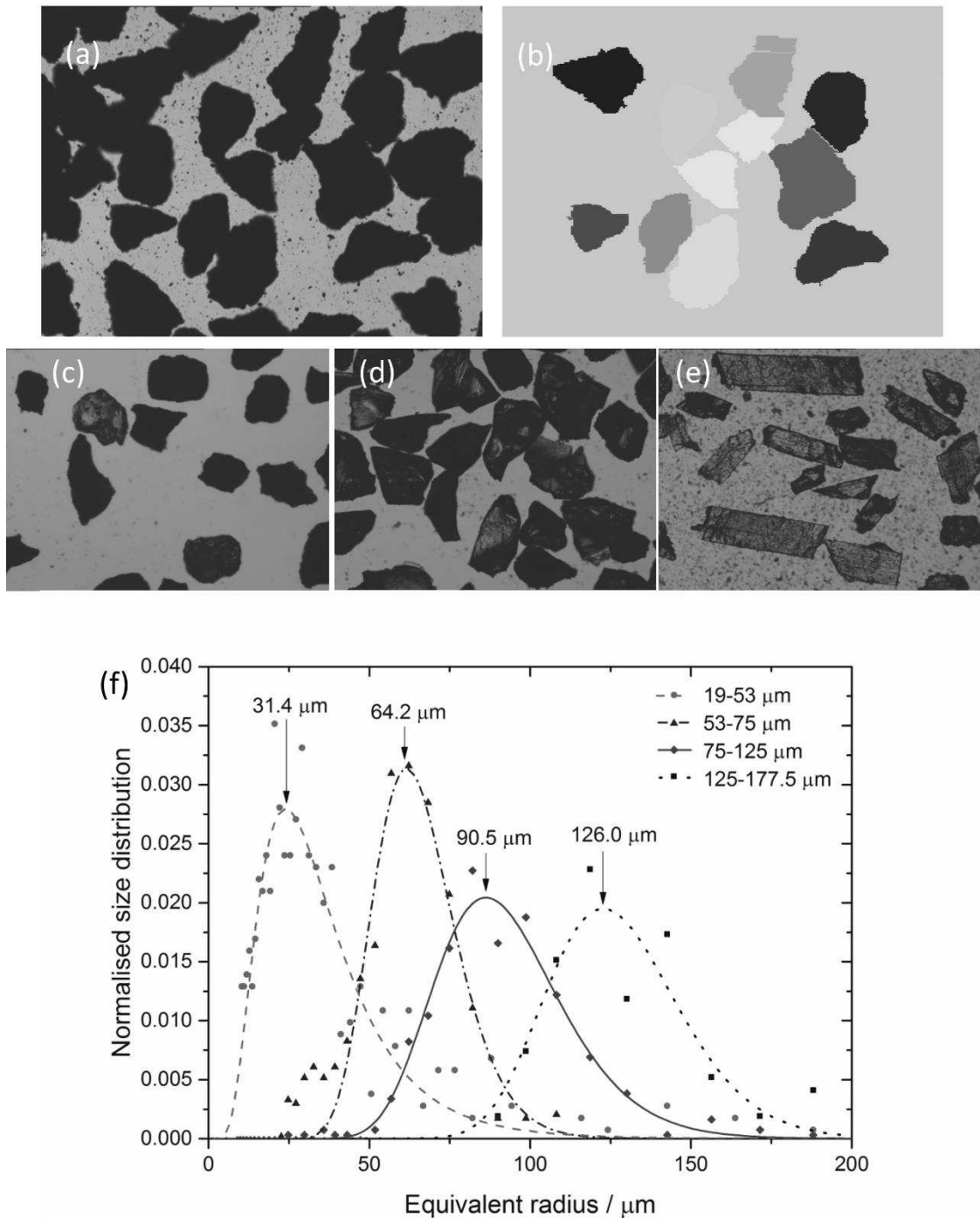
Figure 7.

XRD patterns for synthetic samples produced in this study. Measured data are in black and fits from Rietveld refinement in red. Data have been scaled and offset to show an appropriate scale in each case.

Figure 8.

Typical transmission electron microscope image of the $MgFeSiO_4$ described in this study showing 'folded sheet like' morphology. Insert shows an example of nanocrystalline domains on the sheet surface.

Figure 9.

Example microscope images of the 75-125 μm radius fraction for (a) the Chergach meteorite, (c) the Allende meteorite (d) the peridot olivine and (e) the albite samples. Scales for other images are as for the Chergach sample. Panel (b) shows the particles found by the image analysis software (described in section 3.5) in panel (a). Panel (f) shows a comparison of the measured probability density functions for each of the Chergach size bins investigated here, mean radii are marked and limits set by sieves used for separation are given in the legend.